



Machine learning-enabled spatial multi-omics uncovers lactate-driven targets and tumor microenvironmental reprogramming in cancer



Yingzheng Tan^{1,2,3,15}, Wenliang Tan^{2,3,15}, Yanchao Liang^{4,15}, Yunzhu Long^{1,15}, Shuanghua Chen^{1,5,15}, Qihao Hu⁶, Yangjing Ou¹, Jingli Fu¹, Huan Chen⁷, Fangyuan Ren², Jun Ye⁸, Qing Zhou¹, Sheng Li², Xiaojin He¹, Qianqian Wang⁹, Yueming Shen¹⁰, Haiyuan Lu^{11,12}, Daichao Wu^{3,13}✉, Anbo Gao^{3,14}✉, Xun Chen^{2,3}✉ & Yukun Li^{1,3}✉

Lactate accumulation is a central feature of tumor metabolic reprogramming, yet its spatial and cell-type-specific effects in cancer, such as lung adenocarcinoma (LUAD), remain poorly defined. We integrated single-cell transcriptomics, spatial transcriptomics, spatial metabolomics, and immunofluorescence with TCGA survival data and machine-learning models. High-lactate tumors exhibited increased epithelial and fibroblast abundances, whereas T/NK cells and monocytes/macrophages were enriched in low-lactate samples. Spatial metabolomics revealed cell-type-restricted lactate and pyruvate distributions, with endothelial cells showing minimal lactate accumulation. Endothelial subclusters in high-lactate tissues displayed angiogenic and stress-response signatures and were strongly associated with poor prognosis. Multiple machine-learning frameworks—including random forest, elastic-net regression, SVM, ANN, and decision-tree models—consistently identified endothelial and fibroblast programs as key determinants of high-lactate states and adverse clinical outcomes. Collectively, our multi-omics spatial profiling demonstrates that lactate reshapes the LUAD microenvironment by driving angiogenesis, immune suppression, and prognostic stratification, highlighting lactate-centered pathways as promising therapeutic targets.

Lung adenocarcinoma (LUAD), the most common subtype of non-small cell lung cancer, continues to pose significant clinical challenges despite advances in early detection, molecularly targeted therapies, and immunotherapy^{1,2}. Tumor heterogeneity—spanning genomic, cellular, and metabolic dimensions—underlies both disease progression and variable responses to treatment^{3,4}. Among these, metabolic heterogeneity has emerged as a critical yet underexplored aspect of the tumor microenvironment (TME), with growing evidence that dysregulated metabolites not only reflect tumor cell activity but also actively shape immune responses, angiogenesis, and therapeutic resistance^{5,6}.

Lactate, traditionally regarded as a metabolic byproduct of aerobic glycolysis (the Warburg effect), is now recognized as a central signaling molecule and immunometabolic regulator in cancer^{7–9}. Elevated lactate levels are characteristic of many solid tumors, including LUAD, and contribute to an acidic, immunosuppressive microenvironment. High

extracellular lactate impairs T cell proliferation and function, skews macrophages toward tumor-supportive M2-like phenotypes, and promotes angiogenesis by activating endothelial cells through HIF-1 α -dependent pathways^{10–12}. Furthermore, lactate serves as an alternative fuel for oxidative cancer cells and stromal components, reinforcing the adaptability of tumor metabolism⁷. Despite these insights, the spatial and functional heterogeneity of lactate within LUAD tumors remains poorly characterized. Emerging spatial metabolomics studies suggest that lactate is not uniformly distributed across tumor regions, with areas of high concentration correlating with hypoxia, stromal remodeling, or immune exclusion^{10,13}. Yet, the biological consequences of these lactate gradients—particularly their influence on immune-vascular crosstalk—are largely unknown.

To address this gap, high-resolution, spatially resolved approaches are needed to elucidate how lactate heterogeneity drives regional differences in cell composition, metabolic state, and cell-cell communication. An

integrative multi-omics strategy combining single-cell RNA sequencing (scRNA-seq), 10X Visium spatial transcriptomics, and mass spectrometry-based spatial metabolomics offers a powerful framework to decode the interplay between metabolic heterogeneity and microenvironmental dynamics. Such integration can help pinpoint how lactate-rich niches affect the recruitment, activation, and positioning of immune and vascular cells, as well as how these interactions contribute to LUAD progression or treatment resistance.

In this study, we investigated the role of lactate heterogeneity in shaping the LUAD microenvironment by leveraging multi-modal profiling of surgically resected LUAD tissues stratified by systemic lactate levels. Tumor samples from patients with high or low circulating lactate are subjected to scRNA-seq, spatial transcriptomics, and spatial metabolomics to characterize cellular, molecular, and metabolic features at high resolution. Our central hypothesis is that lactate-rich tumor regions display distinct immune-vascular configurations and metabolic programs compared to lactate-poor regions, driven by local gradients in metabolite availability. By integrating these data modalities, we constructed a comprehensive spatial atlas of lactate-driven metabolic reprogramming and identified molecular networks linking lactate heterogeneity to immune suppression and vascular remodeling, informing precision strategies for patients with metabolically distinct LUAD subtypes.

Results

Single-cell transcriptomics profiling reveals distinct cellular and molecular features associated with lactate levels in LUAD sample

To investigate the impact of lactate heterogeneity on the tumor microenvironment of LUAD, we performed an integrative analysis combining scRNA-seq, spatial transcriptomics, and spatial metabolomics on tumor samples from patients with high- or low-lactate levels ($n = 3$ per group). As illustrated in Fig. 1a, each sample underwent parallel processing for three platforms to enable multi-dimensional characterization of transcriptomic and metabolic features. We first analyzed the scRNA-seq data to characterize the cellular landscape of LUAD tumors under different lactate conditions. UMAP dimensionality reduction revealed distinct clustering patterns between high- and low-lactate groups (Fig. 1b), suggesting that intratumoral lactate levels are associated with global transcriptional divergence across cell populations. This observation indicates that metabolic heterogeneity may contribute to shaping cellular states within the tumor microenvironment. Next, we performed cell type annotation based on canonical marker genes, including *EPCAM*, *KRT8*, and *CDH1* for epithelial cells; *CD3G*, *CD3D*, and *NKG7* for T/NK cells; and *PECAM1*, *CDH5*, and *VWF* for endothelial cells (Fig. 1c). A total of nine major cell types were identified across all samples, including T/NK cells, monocytes/macrophages, epithelial cells, fibroblasts, mast cells, endothelial cells, plasma cells, B cells, and neutrophils (Fig. 1d). The predominant populations were epithelial cells, fibroblasts, T/NK cells, and monocytes/macrophages, indicating that LUAD tumors harbor a complex microenvironment composed of both immune and stromal components that may dynamically respond to metabolic cues. Comparative analysis revealed that high-lactate tumors exhibited increased proportions of fibroblasts and epithelial cells, whereas low-lactate tumors showed higher frequencies of T/NK cells and monocytes/macrophages (Fig. 1e). These differences imply that elevated lactate levels may promote epithelial expansion and fibroblast activation—hallmarks of a more proliferative and desmoplastic tumor phenotype—while suppressing immune cell infiltration and antigen surveillance. Conversely, the low-lactate group exhibited a more immune-infiltrated profile, potentially reflecting a microenvironment more permissive to antitumor immune responses.

Further differential gene expression (DEG) analysis revealed that *HSPA1B* was upregulated in T/NK cells from high-lactate LUAD, while *SFTPC* and *SCGB3A1* were more highly expressed in T/NK cells from the low-lactate group (Fig. 1f). Gene Ontology (GO) enrichment analysis showed that upregulated genes in high-lactate T/NK cells were

predominantly associated with pathways such as “response to unfolded protein” and “response to copper and zinc ions (Fig. 1g),” suggesting that elevated lactate levels may impose metabolic or oxidative stress, leading to activation of protein-folding stress responses and metal ion detoxification mechanisms. Conversely, genes downregulated in these cells were enriched for pathways involved in “viral transcription,” “translational initiation,” and “antigen processing and presentation (Fig. 1h),” indicating a potential suppression of antiviral and antigen-presenting functions under lactate-rich conditions. These results suggest that high-lactate exposure may impair the immune surveillance capacity of T/NK cells by promoting stress adaptation at the expense of immune function. In endothelial cells from high-lactate tumors (Supplementary Fig. 1a), upregulated genes were enriched in GO terms such as “lymph vessel development” and “angiogenesis,” while downregulated genes were associated with “detoxification of copper ion” and “response to metal ion (Supplementary Fig. 1b).” These findings imply that lactate accumulation may enhance angiogenic signaling and lymphatic remodeling, which are critical for LUAD progression and metastasis, while simultaneously suppressing endothelial detoxification capacity, potentially reflecting a trade-off between vascular expansion and homeostatic maintenance under metabolic stress. In B cells, genes upregulated in the high-lactate group were significantly enriched in “immune response” and “antigen processing and presentation (Supplementary Fig. 1c),” whereas downregulated genes were involved in “response to unfolded protein” and “response to calcium ion (Supplementary Fig. 1d).” This pattern suggests that B cells in high-lactate tumors may remain immunologically active but experience reduced ER stress and calcium-mediated signaling. Together, these observations indicate that lactate may exert cell-type-specific regulatory effects: promoting immune suppression and stress responses in T/NK cells, driving angiogenic remodeling in endothelial cells, and selectively modulating humoral immune function in B cells. Subsequent copy number variation (CNV) analysis revealed that tumors in the high-lactate group exhibited globally elevated CNV levels compared to those in the low-lactate group (Supplementary Fig. 1e). Notably, epithelial cells in high-lactate tumors showed significantly higher CNV burden than their counterparts in the low-lactate group (Supplementary Fig. 1f). This finding suggests that elevated lactate levels may be associated with increased genomic instability in epithelial cells, potentially promoting malignant transformation and clonal expansion. Such CNV accumulation under metabolic stress could reflect a more aggressive tumor phenotype and may contribute to therapy resistance or immune evasion.

Cell–cell communication analysis revealed a marked increase in the number of interactions between epithelial cells (epithelial–epithelial) and between epithelial and endothelial cells (epithelial–endothelial) in the high-lactate group compared to the low-lactate group (Supplementary Fig. 2a). This enhancement suggests that elevated lactate levels may facilitate epithelial networking and vascular crosstalk, which are known to promote tumor growth, neovascularization, and microenvironment remodeling. In terms of interaction strength, the communication between fibroblasts and monocytes/macrophages was notably stronger in the high-lactate group, and the overall interaction intensity between endothelial cells and all other cell types was consistently elevated under high-lactate conditions (Supplementary Fig. 2b). These findings indicate that lactate-rich environments may promote fibro-inflammatory signaling and endothelial activation, both of which are critical for extracellular matrix remodeling and angiogenesis in tumor progression. Globally, several signaling pathways—including VEGF, ApoE, WNT, PARs, PTN, and TGF- β —exhibited increased intercellular communication activity in high-lactate tumors (Supplementary Fig. 2c). These pathways are known to be involved in cell proliferation, immune regulation, and vascular development, underscoring lactate’s role in reinforcing protumorigenic signaling networks within the tumor microenvironment. Interestingly, the MHC-I signaling pathway showed enhanced interactions between T/NK cells and other cell types in the high-lactate group, while this pathway was weaker in the low-lactate group (Supplementary Fig. 2d, e). This may reflect compensatory upregulation of antigen presentation under metabolic stress, although it may also indicate a

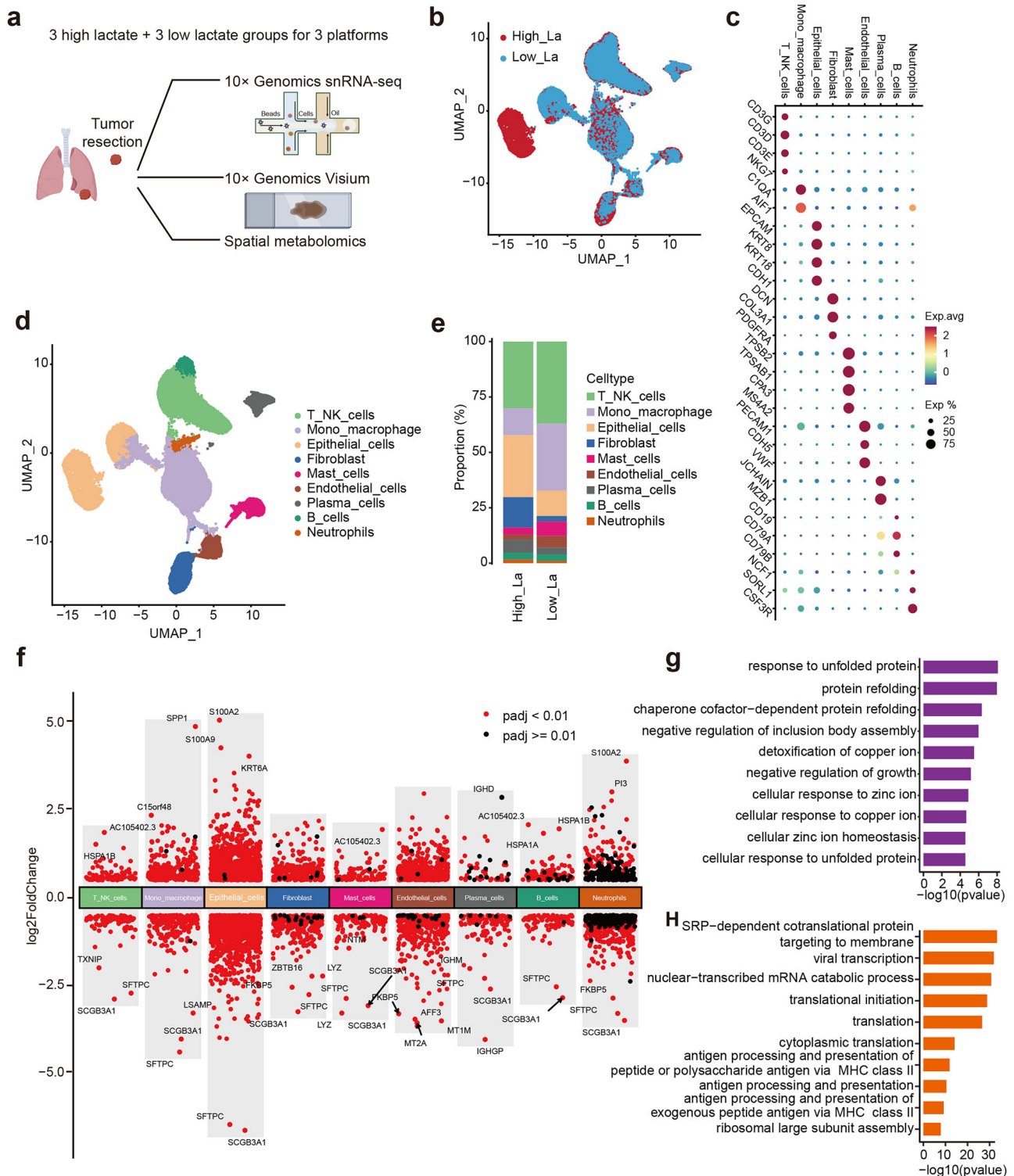


Fig. 1 | Overview of multi-omics profiling in LUAD tissues. a Schematic of the sample collection and multi-omics integration. **b** UMAP visualization showing single-cell clustering from high-/low-lactate (High_La/Low_La) LUAD tissues. **c** Defined markers for each cell types. **d** UMAP visualization showing eight cell types

in LUAD tissues. **e** Percentage of each cell types in high-/low-lactate LUAD tissues. **f** Volcano plots highlighting DEGs (adjusted $p < 0.01$, $|\log_2FC| > 0.5$) in specific cell types between high- and low-lactate LUAD tissues. Top 10 enriched pathways of upregulated (**g**) and downregulated (**h**) genes in T/NK cells.

dysfunctional or exhausted T cell phenotype. For the MHC-II pathway, interactions were stronger among monocytes/macrophages and between monocytes/macrophages and B cells in the high-lactate tumors (Supplementary Fig. 2f, g), whereas these interactions were significantly more pronounced in the low-lactate group. Additionally, fibroblast-mediated MHC-II signaling was observed in both groups, albeit to varying extents.

These trends suggest that lactate may reprogram antigen-presenting pathways in a cell type-specific manner, potentially altering immune activation thresholds and inflammatory tone. Taken together, these findings indicate that elevated lactate levels reshape the intercellular communication landscape of LUAD. This lactate-driven reorganization of cellular interactions may contribute to an immune-suppressive and pro-angiogenic tumor

microenvironment, facilitating disease progression and potentially limiting immunotherapeutic efficacy.

Monocytes/macrophages in lactate-enriched LUAD microenvironments

Monocytes and macrophages are central regulators of immune homeostasis and inflammation within the tumor microenvironment (TME)¹⁴. In LUAD, they play dual roles—participating in anti-tumor immunity or, conversely, facilitating tumor progression through immunosuppressive polarization, angiogenesis, and extracellular matrix remodeling^{15,16}. Increasing evidence suggests that metabolic cues, particularly lactate accumulation, can profoundly reshape the phenotype and function of tumor-associated macrophages (TAMs)^{17,18}. To investigate this, we performed a comprehensive characterization of monocytes/macrophages under differential lactate conditions. Our DEG analysis revealed that, in high-lactate LUAD samples, genes upregulated in monocytes/macrophages were significantly enriched in GO terms related to “cytokine-mediated signaling pathways” and “inflammatory response (Fig. 2a).” This suggests that elevated lactate levels may enhance pro-inflammatory activation states or alter cytokine secretion profiles, potentially contributing to an immunomodulatory TME. In contrast, downregulated genes were enriched in pathways associated with “surfactant homeostasis” and “response to bacterium (Fig. 2b),” indicating a shift away from tissue maintenance and pathogen defense functions, and reflecting a metabolically driven reprogramming toward tumor-supportive phenotypes. KEGG pathway analysis further showed that genes upregulated in high-lactate monocytes/macrophages were enriched in pathways such as “cell cycle,” “phagosome,” and “apoptosis (Supplementary Fig. 3a),” suggesting increased proliferative and phagocytic activity, along with altered cell turnover. Downregulated genes, on the other hand, were enriched in “tight junction” and “focal adhesion” pathways (Supplementary Fig. 3b), implicating a potential loss of structural integrity and reduced interaction with the extracellular matrix, which may facilitate macrophage mobility and plasticity within the tumor milieu.

To further dissect the heterogeneity within this population, we performed subcluster analysis of monocytes/macrophages and identified ten distinct subtypes (Fig. 2c). Among them, subcluster 5 was significantly enriched in the high-lactate group (Fig. 2d). This subpopulation was characterized by elevated expression of pro-tumor and inflammation-associated genes, including *SPP1*, *CCL2*, *SI00A2*, *TIMP1*, and *MIF* (Fig. 2e). These genes are known to promote tumor progression through angiogenesis, immunosuppression, and matrix remodeling. Functional enrichment analysis indicated that these upregulated genes were primarily involved in glycolytic processes and immune response (Fig. 2f), suggesting that lactate may promote metabolic activation and immunomodulatory programming in this subset. Conversely, subcluster 5 showed reduced expression of *SCGB3A1*, *SFTPC*, *LSAMP*, *CH25H*, and *ZBTB16* (Fig. 2e), which are implicated in epithelial differentiation, anti-inflammatory responses, and cholesterol metabolism. Corresponding enrichment analysis highlighted pathways such as chemotaxis and respiratory gaseous exchange by the respiratory system (Fig. 2g), indicating that subcluster 5 in low-lactate contexts may retain more tissue-supportive or anti-tumor properties. This expression pattern suggests that subcluster 5 may represent a metabolically adapted, tumor-promoting macrophage subtype induced by lactate accumulation. Pseudotime trajectory analysis further confirmed dynamic differences in subcluster 5 differentiation between high- and low-lactate conditions (Fig. 2h, i). Cells from the high-lactate group followed a distinct trajectory, indicating that lactate influences not only the static gene expression profile but also the differentiation and maturation pathways of monocytes/macrophages. This supports the notion that lactate serves as a niche-specific cue driving functional polarization and heterogeneity of TAMs in LUAD.

Cell–cell communication analysis revealed that the *SPP1* signaling pathway was strongly activated in high-lactate samples (Fig. 2j), aligning with its known role in promoting tumor cell migration, immune evasion, and matrix remodeling via macrophage-derived osteopontin (*SPP1*). In

contrast, the EGF signaling pathway was preferentially activated in low-lactate tumors (Supplementary Fig. 3c), suggesting that alternative epithelial–myeloid signaling axes may dominate in more metabolically neutral environments. Collectively, these results indicate that lactate not only shapes the transcriptional identity and differentiation of monocytes/macrophages but also modulates their interaction with surrounding cell types through distinct ligand–receptor networks

Epithelial plasticity in response to lactate accumulation in LUAD

Epithelial cells serve as both the structural and functional foundation of LUAD, where they undergo dynamic phenotypic transitions contributing to tumor initiation, progression, and resistance to therapy. To investigate the impact of intratumoral lactate heterogeneity on epithelial populations, we performed DEG and functional analyses. GO enrichment analysis of epithelial cells from the high-lactate group revealed significant upregulation of genes involved in SRP-dependent co-translational protein targeting to membrane and viral transcription (Fig. 3a), indicating an enhanced secretory activity and possibly increased ER stress or translational burden. These changes may reflect elevated biosynthetic demands associated with tumor growth. In contrast, genes related to surfactant homeostasis and ATP synthesis coupled electron transport were significantly downregulated (Fig. 3b), suggesting impaired pulmonary-specific differentiation and mitochondrial respiratory function, which is consistent with metabolic reprogramming in cancer cells toward glycolysis. KEGG pathway enrichment further revealed that upregulated genes in high-lactate epithelial cells were associated with ferroptosis and the p53 signaling pathway (Supplementary Fig. 4a). The induction of ferroptosis—a form of iron-dependent programmed cell death—may reflect a metabolic vulnerability or compensatory stress response, while activation of the p53 pathway might indicate attempts to regulate cell cycle and DNA damage in a metabolically stressed environment. Conversely, downregulated genes were enriched in cellular senescence and phagosome pathways (Supplementary Fig. 4b), suggesting reduced immunogenic clearance and senescence surveillance, which may facilitate immune evasion and tumor cell survival.

To dissect epithelial cell heterogeneity, subclustering analysis identified 11 epithelial subpopulations (Fig. 3c). Notably, subcluster 5 was markedly enriched in the high-lactate group (Fig. 3d). This subcluster displayed elevated expression of *KRT6A*, *TXN*, *KRT5*, *AKR1C1*, and *AKR1C3*—genes associated with basal-like features, oxidative stress response, and metabolic adaptation (Fig. 3e). Functional enrichment of these upregulated genes pointed to roles in mitochondrial respiratory chain complex I assembly and translational initiation (Fig. 3f), underscoring heightened protein synthesis and mitochondrial remodeling in response to lactate-driven stress. Meanwhile, genes downregulated in subcluster 5 under high-lactate conditions included *SCGB3A1*, *SFTPC*, *SFTPB*, *ZBTB20*, and *NAPSA* (Fig. 3e), all of which are markers of alveolar differentiation and surfactant production. These genes were enriched in pathways related to antigen processing and presentation (Fig. 3g), indicating a loss of epithelial immunogenic function and terminal differentiation—a hallmark of tumor dedifferentiation and immune escape. Pseudotime trajectory analysis further supported these findings by demonstrating distinct developmental trajectories of subcluster 5 cells in high- versus low-lactate conditions (Fig. 3h, i), consistent with lactate-induced phenotypic reprogramming and potentially accelerated tumor evolution.

Cell–cell communication analysis revealed increased activation of several signaling pathways in the high-lactate group, including *SPP1*, *CD99*, *JAM*, *CDH*, and *THBS* (Fig. 3g; Supplementary Fig. 4c), which are involved in cell adhesion, extracellular matrix interaction, and immune modulation. Notably, the *PTPRM* signaling pathway was more active in the low-lactate group (Fig. 3g), suggesting a preserved epithelial structural integrity and cell–cell communication that may be disrupted under high-lactate stress. Together, these findings indicate that elevated lactate levels in LUAD are associated with epithelial dedifferentiation, metabolic rewiring, altered immune crosstalk, and a shift toward more aggressive, stress-adapted cellular states, thereby contributing to tumor progression and therapeutic resistance.

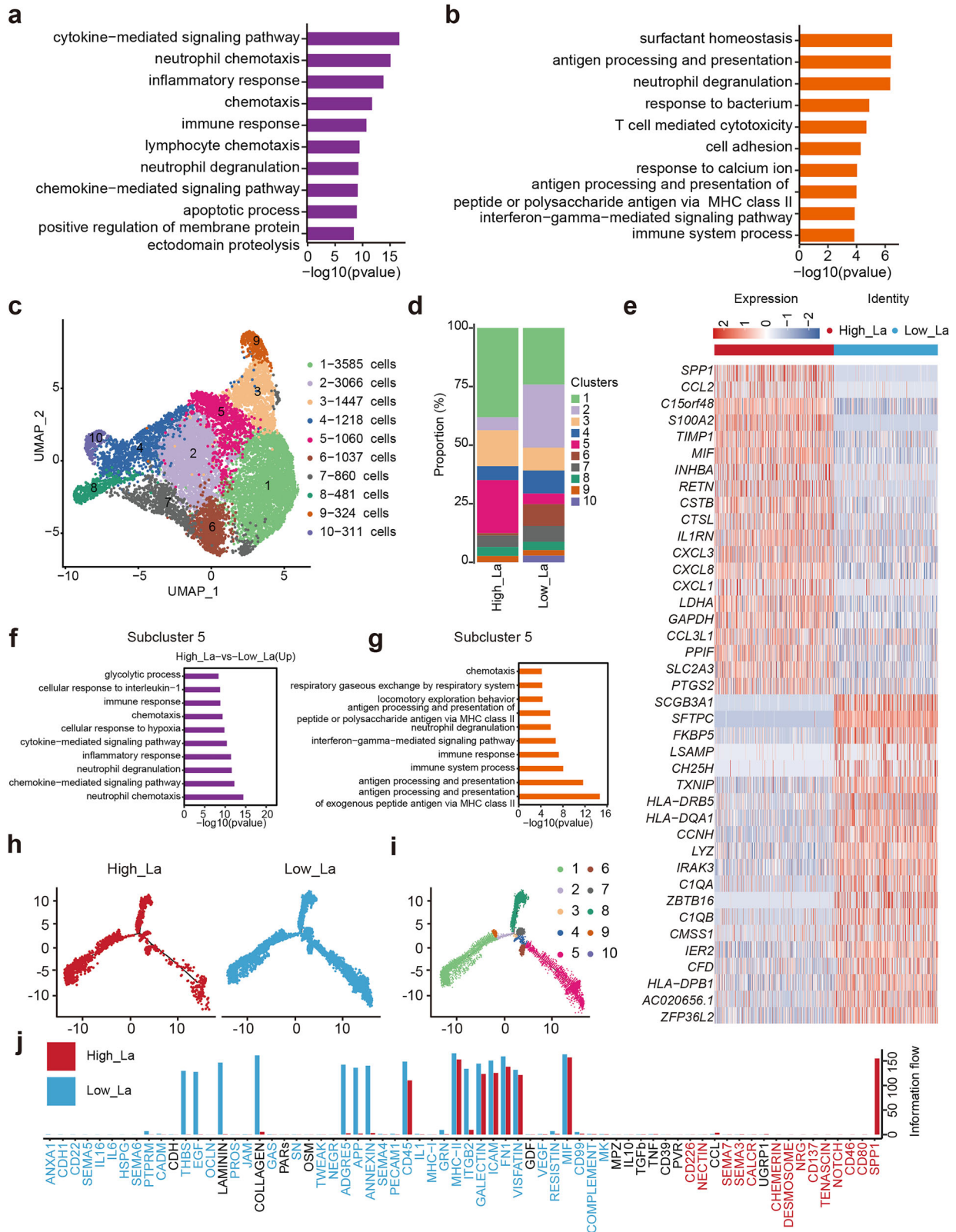


Fig. 2 | Monocyte/macrophage subcluster analysis reveals lactate-associated transcriptional and functional reprogramming. Top 10 enriched pathways of upregulated (a) and downregulated (b) genes in Monocyte/macrophage. c UMAP visualization of monocyte/macrophage populations, identifying 10 transcriptionally distinct subclusters. d Proportions of each subcluster in High_La and Low_La LUAD tissues, highlighting compositional differences. e Heatmaps showing

representative marker gene expression across subcluster 5, including upregulated and downregulated genes. Top 10 enriched pathways of upregulated (f) and downregulated (g) genes in Monocyte/macrophage subcluster 5. Pseudotime analysis identifying cell lineage dynamics in High_La and Low_La tissues (h) and their corresponding cellular subclusters (i). j Information flow plot summarizing predicted intercellular signaling strength in High_La and Low_La conditions.

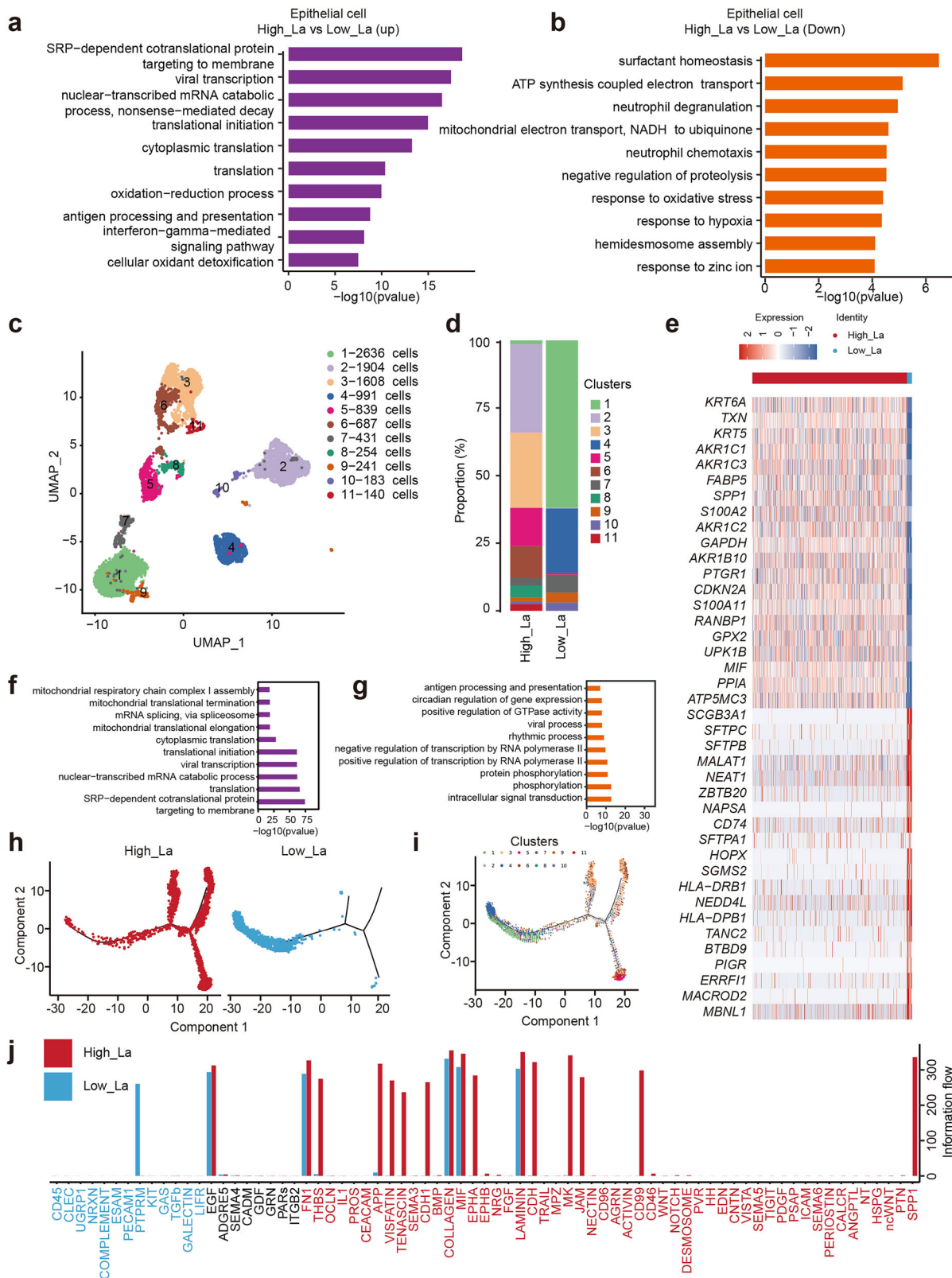


Fig. 3 | Epithelial subcluster profiling highlights lactate-mediated rewiring of transcriptional programs. Top 10 enriched pathways of upregulated (a) and downregulated (b) genes in epithelial cells. c UMAP visualization of epithelial cell populations, identifying 11 transcriptionally distinct subclusters. d Proportions of each subcluster in High_La and Low_La LUAD tissues, highlighting compositional differences. e Heatmaps showing representative marker gene expression across

subcluster 5, including upregulated and downregulated genes. Top 10 enriched pathways of upregulated (f) and downregulated (g) genes in epithelial cell subcluster 5. Pseudotime analysis identifying cell lineage dynamics in High_La and Low_La tissues (h) and their corresponding cellular subclusters (i). j Information flow plot summarizing predicted intercellular signaling strength in High_La and Low_La conditions.

Fibroblast phenotypic transition in a high-lactate tumor microenvironment

Cancer-associated fibroblasts (CAFs) play a pivotal role in shaping the TME of LUAD by modulating extracellular matrix composition, angiogenesis, and immune cell recruitment^{19,20}. Recent studies have shown that metabolic byproducts such as lactate can reprogram fibroblast phenotypes, thereby influencing tumor progression, therapeutic resistance, and immune exclusion²¹. To investigate the role of fibroblasts under differential lactate conditions, we performed DEG and pathway enrichment analyses. GO analysis revealed that fibroblasts from the high-lactate group exhibited upregulation of genes associated with cell adhesion and cellular responses to tumor necrosis factor (Fig. 4a), suggesting enhanced pro-inflammatory and pro-tumorigenic activity. In contrast, downregulated genes were enriched in pathways related to antigen processing and presentation as well as extracellular matrix organization (Fig. 4b), indicating impaired immunoregulatory function and possible structural remodeling. These findings imply that high lactate levels may promote fibroblast activation toward a tumor-supportive, immune-suppressive phenotype. Complementary KEGG pathway analysis demonstrated that upregulated genes in high-lactate fibroblasts were enriched in the NF- κ B signaling pathway (Supplementary Fig. 5a), a key mediator of inflammation and cancer progression. Conversely, genes involved in focal adhesion were significantly downregulated (Supplementary Fig. 5b), suggesting disrupted integrin signaling and potential alterations in cell–matrix interactions that could facilitate cancer cell invasion and tissue remodeling. Subclustering analysis further identified five fibroblast subpopulations (Fig. 4c), among which subcluster 1 was significantly enriched in the high-lactate group (Fig. 4d). This subpopulation was characterized by high expression of *MMP1*, *GREM1*, *COL11A1*, *COL12A1*, and *S100A2* (Fig. 4e), genes associated with protein metabolism and angiogenesis, reflecting an activated myofibroblast-like state conducive to tumor vascularization and matrix remodeling (Fig. 4f). In contrast, genes such as *SFTPC*, *ITGA8*, and *APOC1* were markedly downregulated (Fig. 4e), which were enriched in pathways related to calcium ion transport and response to hyperoxia (Fig. 4g), potentially reflecting a loss of homeostatic or reparative function in these fibroblasts. Pseudotime trajectory analysis further confirmed a distinct lineage progression trajectory of subcluster 1 between high- and low-lactate groups (Supplementary Fig. 5c, d), supporting the notion that lactate accumulation reshapes fibroblast differentiation dynamics.

Cell–cell communication analysis revealed that signaling pathways such as SPP1, THBS, and NOTCH were markedly activated in the high-lactate group (Fig. 4h), indicative of intensified fibroblast-mediated modulation of endothelial and immune cells. Interestingly, the MIF signaling pathway (Supplementary Fig. 5e), often associated with macrophage activation and immune regulation, was predominantly active in the low-lactate group, suggesting an altered inflammatory crosstalk landscape under differential metabolic conditions. Taken together, these findings indicate that elevated lactate levels in the LUAD microenvironment induce a shift in fibroblast function from immune regulation and structural maintenance toward a pro-tumorigenic, pro-angiogenic, and matrix-remodeling phenotype, thereby potentially facilitating tumor progression and resistance to immune surveillance.

Lactate-driven transcriptional reprogramming of endothelial cells in LUAD

Emerging evidence suggests that endothelial cells play a critical role in shaping the TME of LUAD by promoting angiogenesis, facilitating immune cell infiltration, and contributing to metabolic adaptation²². Elevated lactate levels within tumors have been implicated in vascular remodeling and endothelial cell dysfunction^{23,24}, yet the cellular heterogeneity and functional states of endothelial cells under such metabolic stress remain poorly understood. To address this, we performed subclustering analysis of endothelial cells and identified 13 distinct subpopulations (Fig. 5a). Notably, subcluster 1 was significantly enriched in the high-lactate group (Fig. 5b). Cells in this subcluster exhibited high expression of *HSPA1B*, *IGFBP5*,

KCNIP4, *TSHZ2*, and *VEGFC* (Fig. 5c), with enriched pathways related to angiogenesis and extracellular matrix organization (Fig. 5d), suggesting that elevated lactate may promote a pro-angiogenic and matrix-remodeling phenotype in endothelial cells. Conversely, low-expression genes such as *MT2A*, *MT1M*, *LYZM*, and *MT1X* were associated with SRP-dependent co-translational protein targeting to membrane and viral transcription (Fig. 5e), implying a suppression of protein synthesis and stress-related responses in the high-lactate condition.

Pseudotime trajectory analysis further supported the differential state transitions of subcluster 1 between high- and low-lactate groups, indicating lactate-driven endothelial plasticity and possibly a shift toward a more activated or remodeling-prone phenotype (Fig. 5f, g). Inferred cell–cell communication analysis revealed that key signaling pathways including VEGF, NOTCH, and EPHA were markedly enhanced in the high-lactate group, consistent with pro-angiogenic activation (Fig. 5h). In contrast, CXCL and EPHB pathways were predominantly active in the low-lactate condition, reflecting a distinct immune-vascular interaction landscape. These findings suggest that lactate accumulation in the TME promotes endothelial reprogramming toward angiogenic and remodeling states, potentially facilitating tumor progression and immune evasion in LUAD.

Spatial transcriptomic mapping reveals cell-type-specific response in lactate-enriched LUAD tissues

To further investigate the spatial distribution of distinct cell types under high- and low-lactate conditions and to determine how metabolic heterogeneity may shape the tumor microenvironment, we performed spatial transcriptomic analyses. UMAP visualization of spatial transcriptomic profiles revealed discernible differences in cell type compositions between high- and low-lactate LUAD tissues, consistent with our single-cell transcriptomic findings (Fig. 6a). Using label transfer from single-cell RNA-seq data, we mapped the spatial localization of major cell populations across LUAD sections. The spatial landscape of LUAD samples was predominantly composed of epithelial cells, fibroblasts, and monocytes/macrophages, while other cell types such as endothelial cells, plasma cells, and T/NK cells were present at lower frequencies (Fig. 6b, c). This indicates that structural and immune-associated stromal elements are spatially compartmentalized and metabolically influenced in the tumor milieu. Comparative analysis revealed a higher proportion of epithelial cells in high-lactate samples, whereas fibroblasts and monocytes/macrophages were more abundant in low-lactate tissues (Fig. 6d). These differences suggest that lactate levels may influence the recruitment, expansion, or retention of specific cell populations, contributing to tumor progression or immune modulation.

Differential gene expression analysis within spatial transcriptomic datasets further supported this notion (Fig. 6e). In high-lactate regions, monocytes/macrophages exhibited elevated expression of *SPRR3* and *LY6D*, while *SCGB3A1* and *PGC* were significantly downregulated, suggesting a shift toward a pro-inflammatory and matrix-remodeling phenotype. Epithelial cells in the high-lactate group upregulated genes such as *MUC* and *SPRR3*, while downregulating differentiation markers like *SCGB3A1* and *SFTPC*, indicative of a transition toward a less differentiated, potentially more aggressive state. Similarly, fibroblasts displayed increased expression of *SPRR3*, and decreased levels of *SCGB3A1* and *ZBTB16*, suggesting enhanced extracellular matrix deposition and reduced anti-fibrotic signaling. In endothelial cells, upregulation of *KRT5* and *IGHG3* and downregulation of *SCGB3A1* and *PGC* imply activation of angiogenic and stress-response pathways.

To further dissect the metabolic and functional heterogeneity of cell populations within the LUAD microenvironment, we performed subcluster analyses based on spatial transcriptomic data across different lactate conditions. Monocytes/macrophages were categorized into nine spatial subclusters (Supplementary Fig. 6a–d). Among them, subcluster 4 was significantly enriched in high-lactate tissues compared to low-lactate counterparts (Supplementary Fig. 6c). Genes upregulated in this subpopulation under high-lactate conditions were enriched in pathways

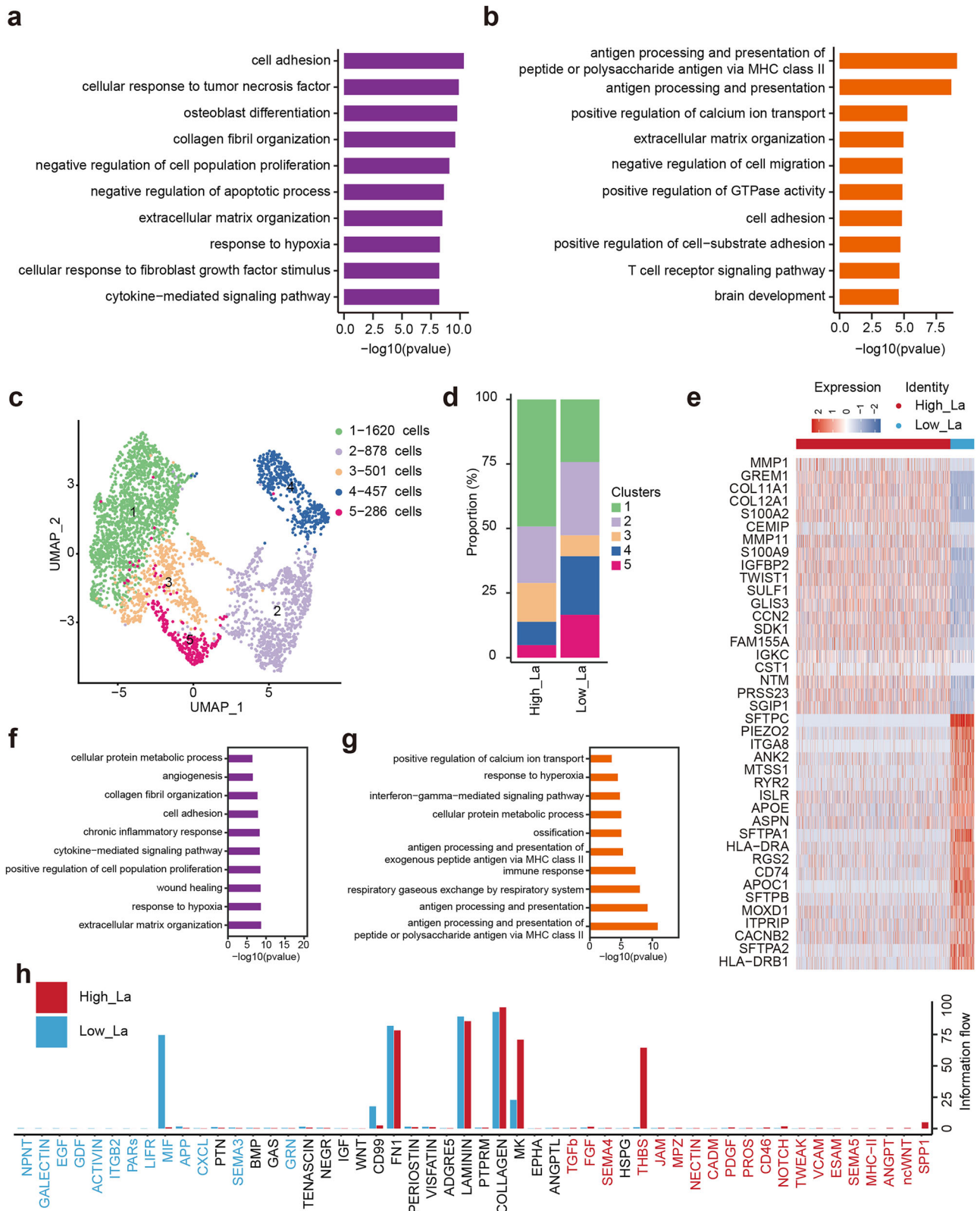


Fig. 4 | Subclustering of fibroblast reveals lactate-driven changes in gene expression and cellular functions. Top 10 enriched pathways of upregulated (a) and downregulated (b) genes in fibroblast. c UMAP visualization of fibroblast populations, identifying 5 transcriptionally distinct subclusters. d Proportions of each subcluster in High_La and Low_La LUAD tissues. e Heatmaps showing

representative marker gene expression across subcluster 1, including upregulated and downregulated genes. Top 10 enriched pathways of upregulated (f) and downregulated (g) genes in fibroblast subcluster 1. h Information flow plot summarizing predicted intercellular signaling strength in High_La and Low_La conditions.

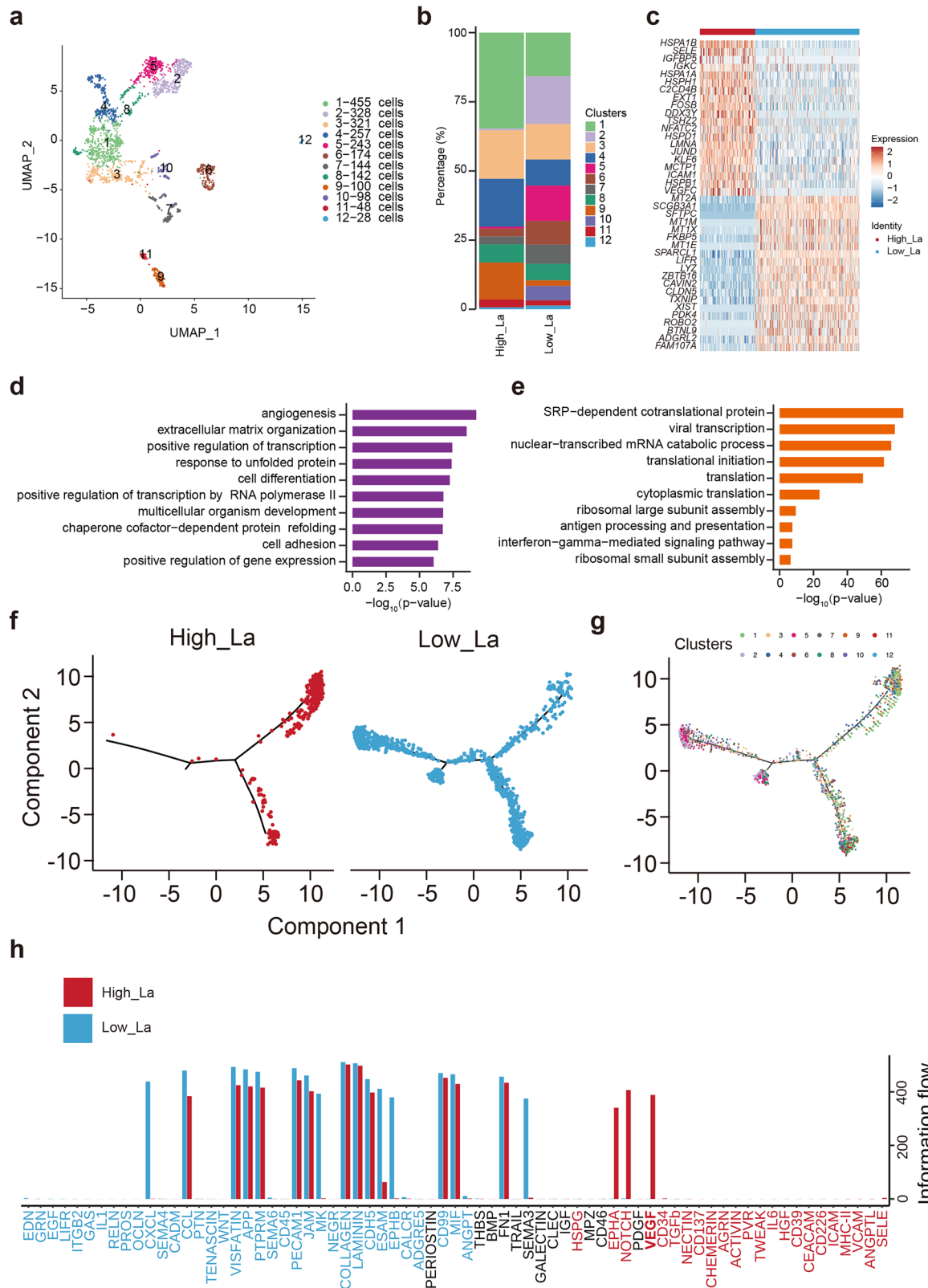


Fig. 5 | Endothelial subclustering reveals lactate-associated transcriptional and functional alterations. **a** UMAP visualization of endothelial populations, identifying 12 transcriptionally distinct subclusters. **b** Proportions of each subcluster in High_La and Low_La LUAD tissues. **c** Heatmaps showing representative marker gene expression across subcluster 1, including upregulated and downregulated

genes. **d** Top 10 enriched pathways of upregulated (d) and downregulated (e) genes in endothelial subcluster 1. Pseudotime analysis identifying cell lineage dynamics in High_La and Low_La tissues (f) and their corresponding cellular subclusters (g). **h** Information flow plot summarizing predicted intercellular signaling strength in High_La and Low_La conditions.

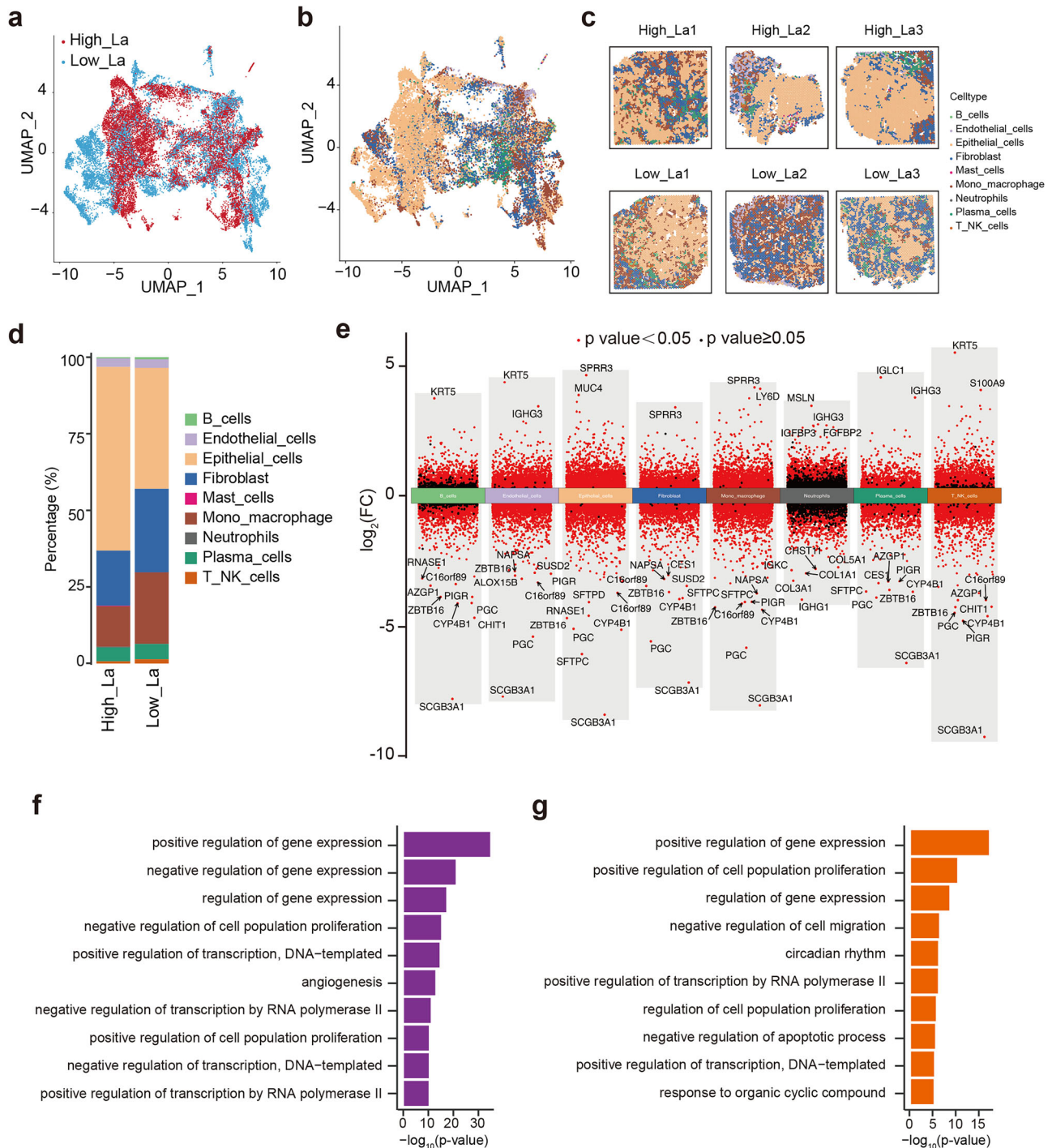


Fig. 6 | 10X visium spatial transcriptomics profiling of high_La and low_La LUAD tissues. **a** UMAP visualization showing bin clustering from high-/low-lactate (High_La/Low_La) LUAD tissues in spatial transcriptomics dataset. **b** UMAP plot illustrating the spatial distribution of eight distinct cell types in LUAD tissues, annotated via label transfer from single-cell RNA-sequencing data. **c** Spatial distribution of eight distinct cell types in LUAD tissues. **d** Percentage of each cell types

in high-/low-lactate LUAD tissues in spatial transcriptomics dataset. **e** Volcano plots highlighting DEGs (adjusted $p < 0.01$, $|\log_2FC| > 1.5$) in specific cell types between high- and low-lactate LUAD tissues. Top 10 enriched pathways of upregulated (**f**) and downregulated (**g**) genes in endothelial cells, based on the intersection of scRNA-seq and spatial transcriptomics datasets.

related to artery morphogenesis and neutrophil chemotaxis (Supplementary Fig. 6e), suggesting a possible role in promoting tumor-associated angiogenesis and inflammatory recruitment. Conversely, downregulated genes were associated with aromatic compound catabolism and the apoptotic process (Supplementary Fig. 6f), implying reduced metabolic detoxification and resistance to cell death. These results indicate that high lactate may reprogram macrophages toward a pro-

tumorigenic and angiogenic phenotype. Additionally, cell-cell communication analysis showed that signaling pathways such as ESAM and OCLN (Supplementary Fig. 6g), which are associated with endothelial tight junctions and vascular integrity, were more active in low-lactate tissues. This may reflect a relatively intact vascular barrier function in low-lactate tumors, potentially limiting tumor dissemination and immune cell infiltration. Epithelial cells were divided into thirteen spatial

subclusters (Supplementary Fig. 7a–d), with subcluster 1 showing higher representation in high-lactate tissues (Supplementary Fig. 7c). Genes upregulated in this cluster were significantly enriched in pathways related to cell cycle progression and DNA repair (Supplementary Fig. 7e), suggesting an increased proliferative and genome maintenance capacity under lactate stress, a hallmark of aggressive tumor behavior. In contrast, downregulated genes were involved in cell migration and angiogenesis (Supplementary Fig. 7f), possibly reflecting a trade-off between proliferative drive and motility under metabolic reprogramming. Notably, signaling pathways such as ANGPTL and VTN (Supplementary Fig. 7g), which are implicated in extracellular matrix remodeling and tumor angiogenesis, were significantly enriched in high-lactate epithelial populations, suggesting enhanced epithelial–stromal communication promoting a tumor-supportive niche. Fibroblasts were classified into twelve subclusters (Supplementary Fig. 8a–d), with subcluster 3 showing marked expansion in high-lactate samples (Supplementary Fig. 8c). Upregulated genes within this subcluster were enriched in angiogenesis and chemotaxis (Supplementary Fig. 8e), suggesting these fibroblasts may contribute to both vascular remodeling and immune cell recruitment. Downregulated genes were associated with axon guidance and response to hypoxia (Supplementary Fig. 8f), indicating a possible suppression of neuroimmune interactions and altered hypoxic adaptation under lactate-rich conditions. Cell communication analysis further revealed enrichment of GABA-B receptor and AGRN (agrin) signaling pathways in the high-lactate fibroblast compartment (Supplementary Fig. 8g). These pathways are increasingly recognized for their roles in modulating immune suppression, extracellular matrix remodeling, and cancer-associated fibroblast (CAF) activation, thereby highlighting a metabolically conditioned stromal network supporting LUAD progression. Together, these results provide spatially resolved evidence that elevated lactate levels induce cell-type- and subcluster-specific transcriptional and signaling adaptations, shaping the tumor microenvironment toward a more proliferative, angiogenic, and immunomodulatory landscape.

To validate these spatial trends, we intersected differentially expressed genes from both the single-cell and spatial transcriptomic analyses. Pathway enrichment of commonly upregulated genes in monocytes/macrophages under high-lactate conditions highlighted Toll-like receptor signaling and extracellular matrix disassembly (Supplementary Fig. 9a), while downregulated genes were enriched in response to bacterium and neutrophil degranulation (Supplementary Fig. 9b), pointing to immunomodulatory reprogramming under metabolic stress. In epithelial cells, upregulated genes were enriched in cornification and epithelial differentiation (Supplementary Fig. 9c), suggesting aberrant maturation processes, whereas downregulated genes mapped to actin filament organization and apoptotic signaling (Supplementary Fig. 9d), implying cytoskeletal instability and evasion of cell death. High-lactate fibroblasts showed enrichment of upregulated genes in collagen fibril organization and cartilage development (Supplementary Fig. 9e), while downregulated genes were associated with gaseous exchange regulation and oxidative stress responses (Supplementary Fig. 9f), indicating fibrotic remodeling and altered metabolic resilience. For endothelial cells, genes related to angiogenesis and regulation of gene expression were upregulated (Fig. 6f), while those associated with cell migration and circadian rhythm were suppressed (Fig. 6g), underscoring a shift toward pathological neovascularization and disrupted homeostatic control. Collectively, these spatial transcriptomic findings demonstrate that elevated lactate levels in LUAD reshape the tumor ecosystem by modulating the distribution, transcriptional programs, and functional states of multiple cell types, thereby potentially promoting tumor progression, immune evasion, and therapeutic resistance.

Spatial multi-omics integration reveals lactate-associated metabolic dynamics in LUAD

To further elucidate the impact of the lactate-enriched microenvironment on metabolic reprogramming in LUAD, we performed an integrative

analysis of spatial transcriptomics and spatial metabolomics data. Lactate, a key metabolite in the Warburg effect, is often elevated in solid tumors and contributes to immunosuppression, angiogenesis, and tumor progression^{25,26}. In our dataset, patients were stratified into high- and low-lactate groups based on their blood lactate concentrations. Spatial metabolomic profiling revealed that lactate abundance was significantly higher in the high-lactate group compared to the low-lactate group (Fig. 7a), consistent with systemic metabolic differences reflective of the TME. This finding supports the hypothesis that systemic lactate levels are mirrored at the tumor tissue level, potentially influencing local cellular behavior. UMAP visualization of spatially resolved cell types showed that mast cells in the low-lactate group were distributed farther from the major cluster (Fig. 7b), indicating potential metabolic or functional divergence under lower lactate exposure. This spatial segregation may suggest reduced metabolic coupling or altered recruitment/function of mast cells in a less glycolytic tumor milieu. Interestingly, cell-type-specific analysis of intratumoral lactate levels showed a differential pattern (Supplementary Fig. 10). In the high-lactate group, monocytes/macrophages, T/NK cells, epithelial cells, and fibroblasts exhibited elevated lactate levels compared to their counterparts in the low-lactate group, suggesting enhanced glycolytic activity or increased lactate uptake by these cells. Paradoxically, endothelial cells in the high-lactate group displayed lower lactate content, implying either a distinct metabolic phenotype, such as increased lactate export, or a compensatory switch toward oxidative metabolism. This discrepancy underscores the metabolic heterogeneity among tumor-resident cells and highlights the unique metabolic state of endothelial cells, which may be involved in maintaining vascular homeostasis despite the surrounding lactate-rich microenvironment.

We further investigated pyruvate, the key metabolite downstream of glycolysis and lactate metabolism (Supplementary Fig. 10). Pyruvate levels were generally higher in the low-lactate group, possibly indicating a reduced conversion of pyruvate to lactate and a more oxidative metabolic profile. Notably, in the high-lactate group, pyruvate levels showed a decreasing trend in monocytes/macrophages, T/NK cells, and epithelial cells, but an increasing trend in fibroblasts. This suggests that different cell types may engage distinct pyruvate–lactate dynamics in response to environmental lactate, with fibroblasts potentially exhibiting enhanced glycolytic flux and intracellular pyruvate accumulation under stress conditions. Conversely, immune and epithelial cells may undergo pyruvate depletion due to its rapid conversion into lactate or its channeling into mitochondrial metabolism. Collectively, these findings suggest that endothelial cells maintain a distinct metabolic identity within LUAD, potentially resisting lactate accumulation and sustaining vessel stability. Meanwhile, other major cell types demonstrate lactate- and pyruvate-associated metabolic rewiring in a cell type-specific manner, reinforcing the functional consequences of lactate gradients within the tumor microenvironment.

Subsequently, we examined the metabolomic differences of endothelial cells between the high- and low-lactate LUAD groups. Spatially resolved metabolite profiling revealed that 10-Acetoxygustoside and fosamprenavir were significantly upregulated in endothelial cells from the high-lactate group (Fig. 7c). Pathway enrichment analysis indicated that these elevated metabolites were predominantly associated with autophagy-related pathways (Fig. 7d, f), suggesting that endothelial cells may activate self-degradative mechanisms to adapt to the metabolically stressed and lactate-rich microenvironment. Autophagy in endothelial cells has been reported to regulate angiogenesis and barrier integrity under tumor-associated hypoxia and nutrient deprivation, which may be particularly relevant in the context of lactate accumulation. Conversely, metabolites such as 2-Chlorohexadecanal and L-lactic acid were downregulated in the high-lactate group (Fig. 7c). Enrichment analysis showed that these downregulated metabolites were mainly associated with choline metabolism in cancer and synaptic pathways (Fig. 7e). The suppression of choline-related metabolism may reflect a shift in membrane lipid remodeling and phospholipid turnover in endothelial cells under lactate stress, potentially altering angiogenic signaling or vascular remodeling. Furthermore, the

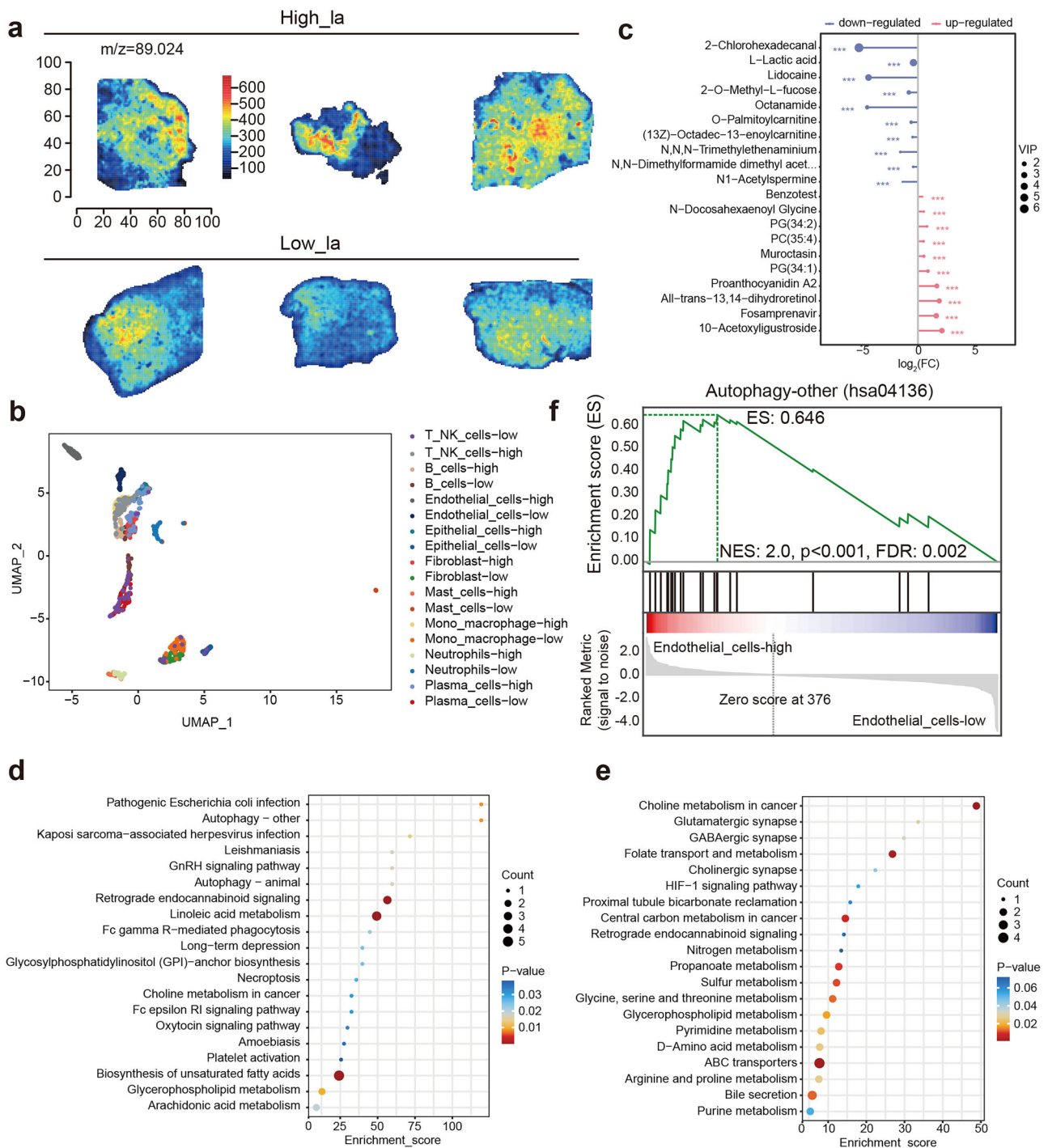


Fig. 7 | Spatial metabolomic and pathway enrichment analysis of endothelial cells in LUAD samples. **a** Spatial distribution of lactate in LUAD samples from high- and low-lactate groups revealed by spatial metabolomics. **b** UMAP visualization showing distinct metabolic profiles across the two groups. **c** Differential expression of

metabolites in endothelial cells between high- and low-lactate LUAD samples. KEGG pathway enrichment analysis of metabolites significantly upregulated (**d**) and downregulated (**e**) in panel (c). **f** GSEA demonstrating enrichment of autophagy-related metabolic pathways in endothelial cells from the high-lactate group.

downregulation of synapse-related metabolic signatures may indicate reduced neurovascular communication or impaired paracrine signaling between endothelial and perivascular cells. Together, these results highlight that endothelial cell in high-lactate LUAD tumors exhibit distinct metabolic adaptations, including enhanced autophagy and altered membrane-associated metabolism, which may support their survival and function in a lactate-enriched tumor microenvironment. These metabolic changes could also contribute to tumor vascular remodeling, immune cell recruitment, or therapy resistance, warranting further functional investigation.

Prognostic relevance of endothelial subpopulations in LUAD
Given the potential regulatory role of lactate on endothelial cells in the LUAD microenvironment, we further investigated the prognostic significance of endothelial subtypes by integrating single cell RNA-seq data with TCGA-LUAD datasets. Specifically, survival analyses were performed to assess associations between the abundance of specific endothelial sub-clusters and clinical outcomes in LUAD patients. The results revealed that endothelial subclusters 1 and 9 were significantly associated with poor prognosis (Fig. 8a, b), such that higher proportions of these subclusters

correlated with reduced overall survival in LUAD patients. Notably, subcluster 9 showed a particularly strong negative correlation with patient survival duration, suggesting that this endothelial phenotype may actively contribute to LUAD progression and resistance to therapy. GO enrichment analysis further supported the distinct functional states of these prognostically unfavorable subpopulations. Subcluster 1 was characterized by upregulation of genes related to cell adhesion and angiogenesis (Fig. 8c), and downregulation of genes involved in oxidation-reduction and lipid metabolism (Fig. 8d), indicating a shift toward a pro-angiogenic, less metabolically flexible endothelial phenotype. Subcluster 9, on the other hand, exhibited increased expression of genes associated with response to unfolded protein and heat stress (Supplementary Fig. 11a), alongside suppression of pathways related to translation initiation and antigen presentation (Supplementary Fig. 11b), suggesting an adaptive stress response potentially contributing to immune evasion and vascular remodeling under metabolic pressure. To further validate these observations, multiplex immunofluorescence staining was conducted using FN1 as an endothelial marker and ENG and MMP2 as vascular markers (Fig. 8d). The staining results confirmed a significant increase in endothelial cells and associated vasculature in the high-lactate LUAD samples, indicating enhanced angiogenic remodeling in response to the lactate-enriched microenvironment. Collectively, these findings suggest that lactate accumulation in LUAD may promote the expansion of pro-angiogenic and stress-adapted endothelial subtypes, which in turn contribute to a more aggressive tumor phenotype and worse patient outcomes. This underscores the clinical relevance of endothelial cell heterogeneity in LUAD and highlights lactate signaling as a potential therapeutic target to disrupt the immunovascular niche that supports tumor progression.

Spatially organized metabolic and transcriptomic remodeling in lactate-high tumor regions

Spatial metabolomics-guided transcriptomic profiling revealed that lactate-high tumor regions exhibit coordinated metabolic and pathway-level reprogramming across major cell types. GSEA on pseudo-bulk profiles demonstrated significant enrichment of angiogenesis and immune-checkpoint programs across epithelial, endothelial, fibroblast, and myeloid populations (Supplementary Figs. 2h, 3d, 4d, and 5f). Metabolic scoring using GSVA further showed elevated glycolysis and reduced oxidative-phosphorylation/hypoxia-response signatures in multiple compartments within lactate-high samples (Supplementary Fig. 12c). GSVA applied specifically to epithelial and fibroblast subsets confirmed enhanced glycolysis and stress-response pathways in epithelial cells, and enriched ECM-remodeling and inflammatory signaling in fibroblasts (Supplementary Fig. 13d). Spatial autocorrelation analysis using Moran's I indicated significant spatial clustering of lactate intensity as well as exhaustion and endothelial-activation scores (Supplementary Data S2). These spatially organized metabolic and immunological states align with increased expression of immune exhaustion markers within endothelial cell at High_La group (Supplementary Fig. 13d). Together, these data demonstrate that lactate accumulation shapes a spatially structured microenvironment characterized by enhanced angiogenesis, metabolic rewiring, and localized immunosuppression.

Endothelial remodeling, altered macrophage polarization, and strengthened immune-vascular interactions in lactate-rich niches

To identify upstream regulators of these changes, SCENIC analysis revealed elevated regulon activity of inflammation- and stress-associated transcription factors (RUNX3, PRDM1, NFKB1, REL, DDIT3, XBP1, ATF4, FOXM1) in endothelial and mono_macrophage subclusters within high-lactate tumors (Supplementary Fig. 12a). Ligand-receptor analysis filtered by statistical significance and effect size highlighted strong lactate-associated increases in APP-CD74, PECAM1-PECAM1, and NAMPT-INSR interactions (Supplementary Fig. 12b). Reference-based scoring of macrophage polarization demonstrated concurrent enrichment of M1-like and M2-like

signatures in lactate-high regions, emphasizing a complex reprogramming rather than a binary shift (Supplementary Fig. 13a). Trajectory inference using Monocle2 identified significant differences in pseudotime and branch selection between lactate-high versus lactate-low endothelial cells, with high-lactate regions preferentially occupying angiogenic lineages (Supplementary Fig. 13b). Spatial proximity analysis—nearest-neighbor distances—revealed altered immune-endothelial spatial relationships in lactate-high tissues (Supplementary Fig. 13f). Collectively, these results demonstrate that lactate-high regions are defined by coordinated endothelial activation, macrophage reprogramming, and intensified immune-vascular communication.

Machine-learning models identify stromal and endothelial determinants of lactate-rich states and link lactate-associated modules to patient prognosis

Several orthogonal machine-learning frameworks were applied to prioritize cell types and transcriptional modules associated with lactate accumulation. A random forest classifier trained to distinguish high- versus low-lactate tumors ranked fibroblasts and endothelial cells as the top contributors, reinforcing their dominant roles in shaping lactate-rich niches (Fig. 9a). Elastic-net regression linking metabolite intensities to gene-module scores achieved an AUC of 0.98 and identified a sparse set of lactate-associated modules retained at λ_{1se} (Fig. 9b–d). An SVM classifier further highlighted top discriminative genes—including PDHB, HK2, EPAS1, MYC, SLC2A1—with results reported in Supplementary Data S4. A shallow artificial neural network trained on deconvolved spatial transcriptomics achieved an AUC of 0.926, with interpretable cell-type-level weights consistent with random forest feature rankings (Fig. 9b). Multinomial logistic regression demonstrated epithelial cells and fibroblasts as significant high-risk contributors to high-lactate status (Supplementary Data S3). To determine clinical relevance, a lactate-related transcriptional score stratified TCGA-LUAD patients by overall survival (Supplementary Fig. 13c). Endothelial subcluster signatures incorporated into an elastic-net Cox model further yielded significant hazard ratios, strengthening the prognostic link (Supplementary Fig. 14a–b). A decision-tree model using lactate-associated gene expression provided an interpretable prognostic classifier, identifying threshold gene levels that separate high-risk versus low-risk patients (Fig. 9g). TCGA projection analyses confirmed preservation of key lactate-associated modules—including glycolysis, endothelial activation, and immunosuppression modules—in a large independent cohort (Supplementary Fig. 13c and Data S5). Together, these models highlight endothelial and stromal compartments as primary determinants of lactate-associated states and establish their prognostic relevance in patient populations.

Discussion

Our study reveals that endothelial cells play a pivotal role in mediating the effects of lactate within the LUAD microenvironment by using multi-omics and machine learning methods. In high-lactate tumors, endothelial cells undergo metabolic and transcriptional reprogramming that favors angiogenesis, as demonstrated by upregulation of *VEGFC*, *IGFBP5*, *THBS*, and other vascular growth regulators. The enrichment of endothelial subclusters associated with angiogenesis and autophagy in high-lactate tumors, along with their correlation to poorer survival outcomes, underscores their contribution to LUAD progression. This aligns with previous reports suggesting that tumor-associated endothelial cells not only form new vasculature but also participate in immune evasion, matrix remodeling, and therapy resistance^{27–29}. Our spatial metabolomics data further demonstrated that these endothelial cells exhibit a unique metabolic profile, characterized by altered choline metabolism and reduced lactate uptake, suggesting a metabolic compartmentalization strategy to support vascular integrity in nutrient-limited environments. Given their central role in shaping the tumor microenvironment, endothelial cells represent a compelling therapeutic target. Strategies such as dual inhibition of lactate transporters and VEGF signaling, reprogramming of endothelial metabolism, or targeting

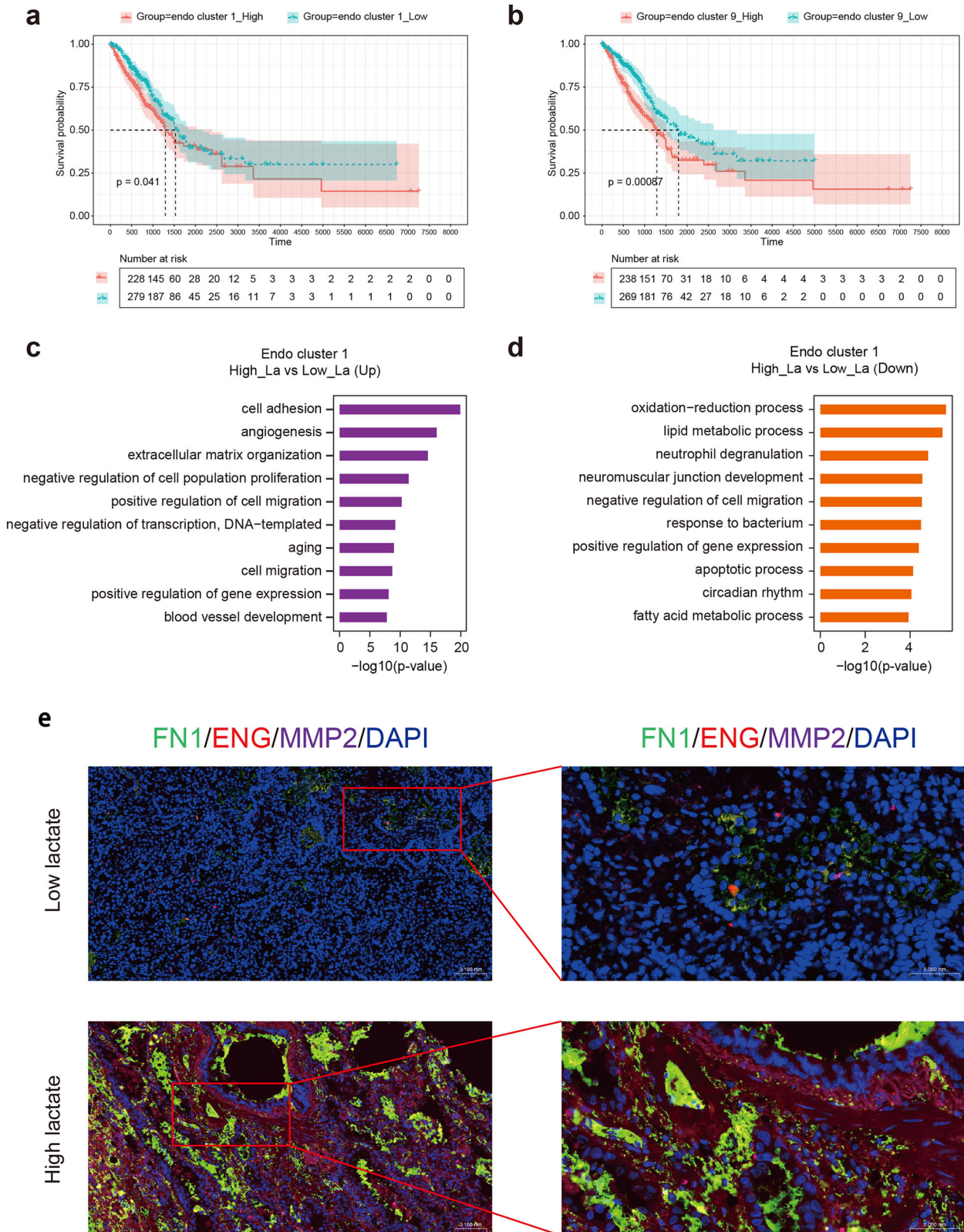


Fig. 8 | TCGA survival analysis of endothelial subtypes in LUAD samples. Kaplan–Meier survival curves showing that endothelial cell subclusters 1 (a) and 9 (b) are significantly associated with poor prognosis in LUAD patients. Top 10 enriched GO pathways of genes upregulated (c) and downregulated (d) in

endothelial cell subcluster 1 from high- vs. low-lactate LUAD samples. **e** Immunofluorescence validation of increased FN1, ENG, and MMP2 expression in high-lactate LUAD samples.

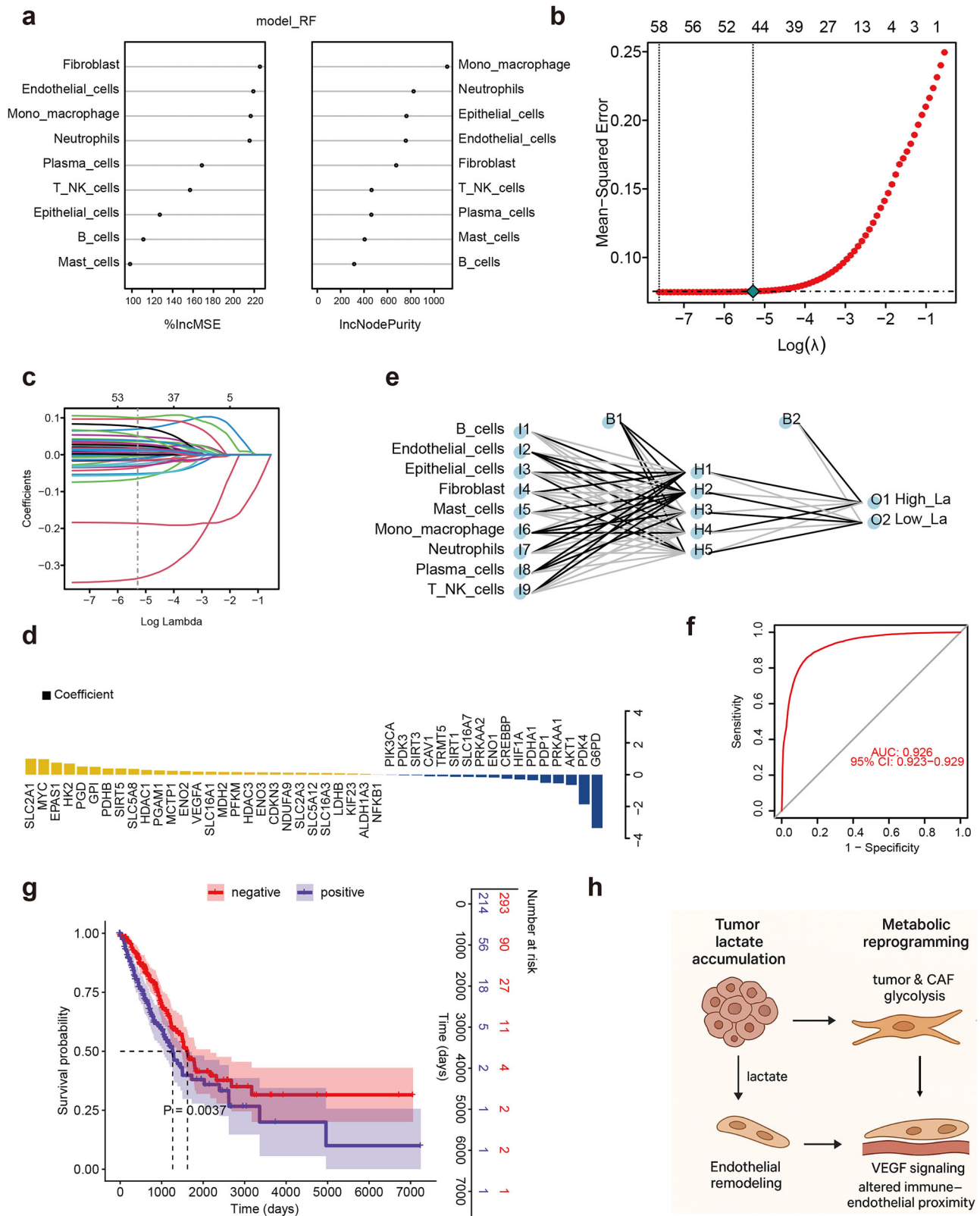


Fig. 9 | Machine-learning frameworks, prognostic modeling, and conceptual summary of lactate-driven microenvironmental remodeling. **a** Random forest classifier distinguishing high- versus low-lactate tumors based on cell-type composition. **b** Mean-Squared Error statistics linking spatial lactate intensities to gene expression module scores. **c** Elastic-net model coefficients highlighting a minimal set of lactate-associated gene modules. **d** Support vector machine (SVM) classifier

identifying the top discriminative genes for lactate status, including PDHB, HK2, EPAS1, MYC, and SLC2A1. **e** Artificial neural network (ANN) model trained on deconvolved spatial transcriptomics. **f** ROC curve for the elastic-net model predicting high-lactate regions. **g** Decision-tree classifier trained on TCGA lactate-associated gene expression. **h** Graphical summary model summarizing the study's findings.

endothelial-specific autophagy pathways could be explored to disrupt angiogenic support in LUAD. Moreover, the use of spatial transcriptomic and metabolomic profiling enables the identification of patients with endothelial-rich, high-lactate tumors who may benefit from such targeted approaches. Future studies should aim to dissect the crosstalk between endothelial cells and other stromal populations under varying metabolic states, and to validate the therapeutic efficacy of endothelial-targeted interventions *in vivo*. Overall, this study provides a comprehensive spatial multi-omics atlas of lactate-related heterogeneity in LUAD. We demonstrate that lactate influences the spatial distribution, transcriptional state, and metabolic profile of multiple cell types, notably epithelial cells, fibroblasts, and endothelial cells. The association of lactate-enriched endothelial subpopulations with pro-angiogenic programs and worse prognosis suggests a novel link between metabolic microenvironment and tumor vascular remodeling. These insights offer potential targets for metabolic or angiogenesis-directed therapies in LUAD.

Methods

The sample size was not determined using statistical methods. All experimental procedures were randomized prior to analysis and evaluated by independent, blinded investigators.

LUAD tissue collection

A total of 60 LUAD paraffin samples were collected from the Zhuzhou Hospital Affiliated to Xiangya School of Medicine (Zhuzhou, Hunan, China) (Approval No. 20240968-03). The ethics standards were formulated in the Helsinki Declaration for these collections and the use of samples. Written informed consent was obtained from each patient, which was approved by the research ethics committee of Zhuzhou Hospital Affiliated to Xiangya School of Medicine.

Single cell RNA sequencing and data processing

Single-cell RNA sequencing procedures were carried out in accordance with prior study. Briefly, freshly resected LUAD tissue specimens were processed under aseptic conditions. Samples were rinsed twice using ice-cold RPMI 1640 medium supplemented with 0.04% bovine serum albumin (BSA) to remove residual blood and debris. The tissue was then transferred into a freshly prepared enzymatic digestion solution and incubated at 37 °C for 30–60 min in a humidified incubator. During incubation, the samples were gently inverted every 5–10 min to ensure uniform digestion. The enzymatic cocktail included RPMI 1640 (Corning, Cat# 10-040-CVR), 0.04% BSA (MACS, Cat# 1000076), and 0.2% Collagenase II (Gibco, Cat# 17101015). Following enzymatic dissociation, the resulting cell suspension was passed through a 40 µm nylon mesh strainer (Falcon, Cat# 352340), one or two times as needed, to remove undigested tissue fragments. The filtered suspension was centrifuged at 300 × *g* for 5 min at 4 °C. The cell pellet was gently resuspended in culture medium, mixed with an equal volume of red blood cell lysis buffer (Miltenyi, Cat# 130-094-183), and incubated on ice for 10 min to lyse erythrocytes. After lysis, the cells were centrifuged again under the same conditions, and the supernatant was discarded. The pellet was washed once more with culture medium and centrifuged at 300 × *g* for 5 min at 4 °C. The final cell pellet was resuspended in 100 µL of RPMI 1640 medium containing 0.04% BSA (Corning, Cat# 10-040-CVR). Single-cell suspension viability and concentration were measured using either a Luna-FL automated fluorescence cell counter (Logos Biosystems, Korea) or trypan blue exclusion with a hemocytometer.

The freshly prepared single-cell suspension was adjusted to a concentration of 700–1200 cells/µL prior to library construction. Single-cell libraries were generated using the 10x Genomics Chromium Next GEM Single Cell 3' Reagent Kit v3.1 (Cat# PN-1000268) in accordance with the manufacturer's instructions. Sequencing was performed on the Illumina NovaSeq 6000 platform using a PE150 strategy.

Raw sequencing data were processed using Cell Ranger (v9.0.0, 10X Genomics), which included demultiplexing, alignment to the human reference genome GRCh38, and quantification of unique molecular

identifiers (UMIs) per barcode. The resulting UMI count matrix was analyzed using the Seurat R package (v4.0.0). Low-quality cells and potential multiplets were excluded based on the following criteria: (1) fewer than 200 detected genes, (2) fewer than 1000 UMIs, (3) $\log_{10} \text{GenesPerUMI} < 0.7$, (4) mitochondrial transcript content $> 10\%$, and (5) hemoglobin transcript content $> 5\%$. Additional doublet filtering was carried out using DoubletFinder (v2.0.3). All QC summaries and raw count matrices for scRNA-seq data are now provided in Supplementary Data S1 and Data Availability section.

Gene expression normalization was performed using Seurat's `NormalizeData` function, applying the "LogNormalize" method: gene counts were scaled to a total of 10,000 per cell and log-transformed. The top 2000 highly variable genes (HVGs) were identified using the `FindVariableFeatures` function with `mean.function = FastExpMean` and `dispersion.function = FastLogVMR`. Dimensionality reduction was conducted using principal component analysis (PCA) via the `RunPCA` function. To correct for batch effects, the Harmony algorithm (`RunHarmony`, Harmony v1.0) was applied.

Graph-based clustering was performed using the `FindClusters` function. Clusters were visualized in two dimensions using Uniform Manifold Approximation and Projection (UMAP) with the `RunUMAP` function. Marker genes for each cluster were identified using the `FindAllMarkers` function (`test.use = "presto"`). Differentially expressed genes (DEGs) between clusters or groups were detected using the `FindMarkers` function, also with the "presto" test. Significance was determined by Bonferroni-adjusted *p* values < 0.05 and absolute \log_2 fold change > 0.58 .

Gene Ontology (GO) and Kyoto Encyclopedia of Genes and Genomes (KEGG) enrichment analyses were conducted based on the hypergeometric distribution using R software (v4.0.3). Sequencing and downstream bioinformatic analysis were performed in collaboration with OE Biotech Co., Ltd. (Shanghai, China).

10X visium spatial transcriptomics profiling and data processing

Freshly obtained LUAD tissue specimens were trimmed into appropriate sizes, and surface moisture was carefully removed using sterile wipers. Samples were embedded in OCT compound (SAKURA, Cat# 4583), snap-frozen on dry ice, and preserved at -80 °C until further processing. OCT-embedded blocks were submitted to OE Biotech Co., Ltd. (Shanghai, China) for spatial transcriptomics library preparation, sequencing, and subsequent analysis. Cryosections of 10 µm thickness were prepared using a Leica CM1950 cryostat at -20 °C. Following the 10x Genomics Visium protocol (CG000614), tissue sections underwent methanol fixation, hematoxylin-eosin (H&E) staining, imaging, and destaining. Probe hybridization and release were carried out according to the manufacturer's instructions (CG000495). Samples were then transferred to Visium CytAssist slides, and libraries were constructed using the Visium CytAssist Spatial Gene Expression for FFPE kit (PN-1000520/21/22/23, depending on species and capture area). Paired-end sequencing (PE100) was performed using the BGI DNBSEQ-T7 platform.

Raw FASTQ files were aligned to the GRCh38 human genome using Space Ranger (v2.0.1, 10x Genomics), and UMI counts were summarized per spatial barcode. Image-based tissue segmentation was performed to distinguish valid capture areas from background. The filtered UMI count matrix was then analyzed using Seurat (v4.1.0) in R. Data normalization and identification of the top 3000 highly variable genes (HVGs) were performed using `sctransform`. Dimensionality reduction was achieved through principal component analysis (PCA) on the log-transformed expression matrix of HVGs. Batch correction was applied using `RunHarmony` from the Harmony package (v1.0).

Graph-based clustering was performed via the `FindClusters` function based on gene expression similarity. Spatial transcriptomic spots were visualized using Uniform Manifold Approximation and Projection (UMAP) via `RunUMAP`. Cluster-specific marker genes were identified using `FindAllMarkers` (`test.use = "bimod"`), and differentially expressed genes (DEGs) were identified with the `FindMarkers` function (`test.use =`

“presto”). Genes with an adjusted p value < 0.05 (Bonferroni correction) and absolute \log_2 fold change > 0.58 were considered significantly differentially expressed. GO and KEGG enrichment analyses were performed using R (v4.0.3), employing a hypergeometric distribution model.

Spatial metabolomics profiling and data processing

LUAD tissue samples were embedded in OCT and stored at -80°C . Serial sagittal cryosections ($10\ \mu\text{m}$, ~ 10 slices) were obtained using a cryostat (Leica CM1950) and mounted onto positively charged desorption plates (Thermo Scientific, USA). Prior to analysis, slides were desiccated at -20°C for 1 h and equilibrated to room temperature for 2 h. Adjacent sections were used for hematoxylin and eosin (H&E) staining.

Mass spectrometry imaging was performed using an AFADESI-MSI system (Beijing Victor Tech, China) coupled with a Q Exactive Orbitrap mass spectrometer (Thermo Scientific, USA). Solvent composition was acetonitrile/water (8:2) for both positive and negative ion modes. Key instrument parameters included: solvent flow rate, $5\ \mu\text{L}/\text{min}$; gas flow rate, $45\ \text{L}/\text{min}$; spray voltage, $7\ \text{kV}$; distance between sprayer and sample, $3\ \text{mm}$; capillary temperature, 350°C ; S-lens voltage, $55\ \text{V}$; resolution, $70,000$; scan range, $m/z\ 70\text{--}1000$; AGC target, $2e6$; injection time, $200\ \text{ms}$. Scanning was conducted at $0.2\ \text{mm}/\text{s}$ in the X-axis with $100\ \mu\text{m}$ vertical steps. Raw MS data were converted to imzML format using imzMLConverter, and processed with MSiReader on MATLAB. Background subtraction and ion image reconstruction were performed using the Cardinal R package. All MSI data were normalized by total ion current (TIC) per pixel. High-resolution H&E images were used to extract region-specific metabolic profiles. Differential metabolites were identified using orthogonal partial least squares-discriminant analysis (OPLS-DA). Variables with a variable importance in projection (VIP) score > 1.0 and a two-tailed Student's t test $p < 0.05$ were considered significant. To further explore spatial metabolic patterns, dimensionality reduction was applied using t-SNE and UMAP algorithms. Spatial clustering was performed using the spatial shrunken centroids clustering (SSCC) method. Metabolite identification was conducted using the pySM pipeline and a custom database (SmetDB, Lumingbio, Shanghai, China) based on AFADESI-detected ion features.

Spatial coordinates from both the transcriptomic barcodes and metabolomic pixel points were mapped to a unified spatial reference system. For each transcriptomic spot, the corresponding metabolomic pixels were identified, and ion intensity values from these pixels were aggregated. This process yielded a re-integrated spatial metabolomics matrix aligned with the transcriptomic spatial layout.

Gene set enrichment analysis (GSEA)

Gene set enrichment analysis was conducted using gene sets derived from the Kyoto Encyclopedia of Genes and Genomes (KEGG) and Gene Ontology (GO) databases. Gene set files were processed via the GSEABase package (v1.44.0), and enrichment analysis was performed using the GSEA algorithm to identify significantly overrepresented pathways and functional terms.

Pseudotime trajectory inference

To explore cellular differentiation trajectories, pseudotime analysis was carried out using the Monocle2 package (v2.9.0). The Seurat-derived object was converted to a CellDataSet format using importCDS. Ordering genes were identified via the differentialGeneTest function (q -value < 0.01). Dimensionality reduction and trajectory inference were performed using reduceDimension and orderCells, respectively, with default parameters. Temporal gene expression dynamics were visualized with the plot_genes_in_pseudotime function.

Intercellular communication analysis

Cell-cell interaction networks were constructed using the CellChat package (v2.1.2). Normalized expression matrices were used to create CellChat objects with createCellChat. Subsequent preprocessing steps—including identification of overexpressed genes and signaling interactions—were

performed using identifyOverExpressedGenes, identifyOverExpressedInteractions, and projectData. Probabilistic inference of signaling pathways was achieved using computeCommunProb, filterCommunication (min.cells = 10), and computeCommunProbPathway. The overall interaction network was summarized via the aggregateNet function.

Copy number variation inference

Copy number variations (CNVs) at the single-cell level were inferred using the inferCNV package (v1.0.4). The analysis was based on gene expression profiles with a cutoff threshold of 0.1. Genes were ordered according to genomic coordinates, and expression values were smoothed using a 101-gene sliding window. Data were mean-centered to normalize expression. Epithelial cells were designated as malignant, while other cell types were used as reference for baseline expression. A denoising step was included to refine the CNV profiles.

Cell-type deconvolution using RCTD

Cell-type composition across spatial transcriptomic bins was inferred using the RCTD package (v1.1.0), based on a reference single-cell RNA-seq dataset in this study. The create.RCTD function was run with default settings, except for the following adjustments: a minimum of one cell per cell type and at least one UMI per spatial bin were required. In the run.RCTD function, the doublet_mode parameter was set to FALSE to disable doublet modeling.

TCGA survival analysis

RNA-seq data and corresponding clinical information for lung adenocarcinoma (LUAD) were downloaded from The Cancer Genome Atlas (TCGA) database. To estimate the relative proportions of endothelial cell within bulk RNA-seq samples, we performed deconvolution analysis using CIBERSORT (R script v1.03), leveraging a single-cell-derived reference. First, cell-type annotation information (column named new_celltype by default) was extracted from the Seurat object, and the log-normalized average expression for each annotated cell type was computed to construct the signature matrix. Concurrently, the bulk RNA-seq expression matrix (in FPKM format) was processed, and genes shared between the bulk and single-cell datasets were retained to generate a matched input matrix. CIBERSORT was then run using the support vector regression (SVR) model to estimate the relative abundance of each cell type. The number of permutations was set to 50 to calculate the empirical p -value indicating the statistical significance of the deconvolution fit for each sample. Quantile normalization was disabled (QN = FALSE) to better accommodate the characteristics of RNA-seq data. The final output included the estimated cell-type proportions for each sample, correlation coefficients, root mean square error (RMSE), and corresponding p -values. Results were visualized using heatmaps and stacked bar plots to display cell composition across samples.

Immunofluorescent staining

LUAD tissue embedding and cryosectioning were performed as described in the spatial transcriptomics protocol. Sections of $10\ \mu\text{m}$ thickness were prepared using a cryostat (Leica CM1950) at -20°C . Multiplex immunofluorescence was conducted using a three-round sequential staining approach. Unless otherwise specified, all steps were carried out under sterile conditions at room temperature. Sections were rinsed with $1\times$ PBS ($5\ \text{min} \times 6$), followed by permeabilization with 0.3% Triton X-100 at 37°C for 30 min and an additional PBS rinse ($3\ \text{min} \times 3$). Endogenous peroxidase was inactivated by incubation with 3% hydrogen peroxide in the dark for 15 min, followed by PBS washes ($5\ \text{min} \times 3$). Tissues were then blocked with 5% BSA for 60 min at 37°C . For each antibody cycle, primary antibodies (diluted appropriately) were applied overnight at 4°C , followed by 2 h at 37°C . After PBS washes, HRP-conjugated secondary antibodies ($50\ \mu\text{L}$) were added for 30 min at 37°C . Tyramide signal amplification was performed for 10 min, followed by three PBS rinses. Antibody removal was achieved by two sequential incubations with prewarmed elution buffer at 37°C for 20 min each, with intermediate PBS washes ($5\ \text{min} \times 3$). This

procedure was repeated for all three targets. Following the final staining round, DAPI (5 µg/mL) was used to label nuclei at 37 °C for 10 min. Slides were then washed in PBS and mounted with a glycerol-based antifade medium (Abiowell, Cat# AWI0178), and stored in the dark prior to imaging. Antibodies used in this study were from MMP2 (Abiowell, #AWA59147), ENG (Proteintech, #10862-1-AP), and FN1 (Abiowell, #AWA10327).

Images were acquired using a fluorescence microscope (Motic BA210T) at 400× magnification or scanned using a panoramic digital imaging system. Fluorescence signals were detected using appropriate filters, with green, orange, and purple indicating target markers and blue representing nuclear DAPI staining. Image analysis was performed using ImageJ and HALO software.

Regulon inference and activity analysis

Transcription factor (TF) regulons were inferred using the pySCENIC workflow. Briefly, pySCENIC identifies co-expression modules consisting of TFs and their putative target genes, followed by motif enrichment-based pruning to generate high-confidence regulons. For each cell, regulon activity scores (RAS) were calculated using the AUCell algorithm to quantify the activity of individual regulons. To assess the cell-type specificity of predicted regulons, we computed the regulon specificity score (RSS), which measures the degree to which a regulon is selectively activated in a given cell population. In addition, the connection specificity index (CSI) was used to evaluate the regulatory similarity between pairs of regulons; regulons with high CSI values were considered to be functionally related and potentially co-regulating downstream gene programs.

Elastic net regression

Elastic net regression was performed using the glmnet package to identify key features associated with lactate levels. A tenfold cross-validation scheme was implemented to determine the optimal regularization parameter. For each model, the coefficients were estimated for the selected feature set and weighted accordingly during model fitting. The value of λ corresponding to λ_{1se} —the most regularized model within one standard error of the minimum cross-validated error—was selected to balance sparsity and model performance. Features with non-zero coefficients at λ_{1se} were considered the most robust predictors and were retained as key variables.

Random forest classification

Random forest classification was conducted using the randomForest package as an ensemble learning framework based on decision trees. Bootstrap sampling with replacement was applied to generate multiple training subsets, and individual decision trees were built on each resampled dataset. At each split, a random subset of predictor variables was chosen without replacement, and the optimal splitting feature was selected based on the highest reduction in node impurity. For this study, a total of 1000 classification trees were constructed with 50 iterations of perturbation to ensure stability. Feature importance was evaluated using the %IncMSE metric, which quantifies the increase in prediction error upon permutation of each feature.

Support vector machine (SVM) and recursive feature elimination

Support vector machine analysis was performed using the e1071 package. To identify the most informative biomarkers related to lactate status, we applied SVM-Recursive Feature Elimination (SVM-RFE), an iterative feature selection method that eliminates features with the smallest contribution to the SVM decision boundary. At each iteration, the SVM model was retrained on the reduced set of variables, and features were ranked based on their weight vectors. This procedure allowed the identification of a minimal subset of genes with the highest discriminative power for differentiating lactate-high and lactate-low conditions.

Artificial neural network (ANN) model development and validation

An artificial neural network model was developed using the neuralnet package to evaluate the diagnostic relevance of lactate-related cellular states

across subpopulations. Based on the variation in lactate levels across clusters, we computed cell-type scores as input features for ANN training. The network architecture consisted of one hidden layer with five neurons, and model weights were estimated using backpropagation. A diagnostic ANN classifier was then constructed using the derived “cell scores,” and model performance was assessed using the area under the ROC curve (AUC) to quantify predictive accuracy.

Data availability

All multi-omics data generated in this study have been deposited in the National Genomics Data Center (NGDC) database (<https://ngdc.cnbc.ac.cn/gsub/>) (HRA015629 dataset) and METASPACE database (<https://metaspace2020.org/datasets?prj=333c0688-d56c-11f0-a049-2345975d66f5>). For any further information necessary to reproduce or reanalyze the findings, please contact the lead author upon reasonable request (Yukun Li, email: yukun_li@csu.edu.cn).

Code availability

No custom code was developed for this study; all software and scripts used are publicly accessible.

Received: 9 August 2025; Accepted: 14 December 2025;

Published online: 30 December 2025

References

- Harada, G., Yang, S. R., Cocco, E. & Drilon, A. Rare molecular subtypes of lung cancer. *Nat Rev Clin Oncol* **20**, 229–249 (2023).
- Lahiri, A. et al. Lung cancer immunotherapy: progress, pitfalls, and promises. *Mol Cancer* **22**, 40 (2023).
- Bhat, G. R. et al. Cancer cell plasticity: from cellular, molecular, and genetic mechanisms to tumor heterogeneity and drug resistance. *Cancer Metastasis Rev* **43**, 197–228 (2024).
- Vitale, I., Shema, E., Loi, S. & Galluzzi, L. Intratumoral heterogeneity in cancer progression and response to immunotherapy. *Nat Med* **27**, 212–224 (2021).
- Chen, C., Han, P. & Qing, Y. Metabolic heterogeneity in tumor microenvironment - A novel landmark for immunotherapy. *Autoimmun Rev* **23**, 103579 (2024).
- Demicco, M., Liu, X.-Z., Leithner, K. & Fendt, S.-M. Metabolic heterogeneity in cancer. *Nat Metab* **6**, 18–38 (2024).
- Jin, M., Cao, W., Chen, B., Xiong, M. & Cao, G. Tumor-derived lactate creates a favorable niche for tumor via supplying energy source for tumor and modulating the tumor microenvironment. *Front cell developmental Biol* **10**, 808859 (2022).
- Li, X. et al. Lactate metabolism in human health and disease. *Signal Transduct Target Ther* **7**, 305 (2022).
- Llibre, A., Kucuk, S., Gope, A., Certo, M. & Mauro, C. Lactate: A key regulator of the immune response. *Immunity* **58**, 535–554 (2025).
- Gao, Y. et al. Tumor microenvironment: Lactic acid promotes tumor development. *J Immunol Res* **2022**, 3119375 (2022).
- Barba, I., Carrillo-Bosch, L. & Seoane, J. Targeting the Warburg effect in cancer: Where do we stand? *Int. J. Mol. Sci.* **25**, <https://doi.org/10.3390/ijms25063142> (2024).
- Lv, X., Mao, Z., Sun, X. & Liu, B. Intratumoral heterogeneity in lung cancer. *Cancers (Basel)* **15**, <https://doi.org/10.3390/cancers15102709> (2023).
- Cai, H., Zhang, F., Xu, F. & Yang, C. Metabolic reprogramming and therapeutic targeting in non-small cell lung cancer: Emerging insights beyond the Warburg effect. *Front Oncol* **15**, 1564226 (2025).
- Huang, R., Kang, T. & Chen, S. The role of tumor-associated macrophages in tumor immune evasion. *J Cancer Res Clin Oncol* **150**, 238 (2024).
- Zhang, H. et al. Integrative single-cell analysis of LUAD: elucidating immune cell dynamics and prognostic modeling based on exhausted CD8+ T cells. *Front Immunol* **15**, 1366096 (2024).

16. Grant, G. & Ferrer, C. M. The role of the immune tumor microenvironment in shaping metastatic dissemination, dormancy, and outgrowth. *Trends Cell Biology*, <https://doi.org/10.1016/j.tcb.2025.05.006> (2025).
17. Colegio, O. R. et al. Functional polarization of tumour-associated macrophages by tumour-derived lactic acid. *Nature* **513**, 559–563 (2014).
18. Tao, H., Zhong, X., Zeng, A. & Song, L. Unveiling the veil of lactate in tumor-associated macrophages: a successful strategy for immunometabolic therapy. *Front Immunol* **14**, 1208870 (2023).
19. Zheng, L. et al. Cancer-associated fibroblasts: a pivotal regulator of tumor microenvironment in the context of radiotherapy. *Cell Commun Signal* **23**, 147 (2025).
20. Wright, K., Ly, T., Kriet, M., Czirok, A. & Thomas, S. M. Cancer-associated fibroblasts: Master tumor microenvironment modifiers. *Cancers (Basel)* **15**, <https://doi.org/10.3390/cancers15061899> (2023).
21. Gu, X. et al. Lactate-induced activation of tumor-associated fibroblasts and IL-8-mediated macrophage recruitment promote lung cancer progression. *Redox Biol* **74**, 103209 (2024).
22. Zhang, M., Liang, Y. & Song, P. COL3A1-positive endothelial cells influence LUAD prognosis and regulate LUAD carcinogenesis by NCL-PI3K-AKT axis. *J Gene Med.* **26**, e3573 (2024).
23. Lee, H. W. et al. Endothelium-derived lactate is required for pericyte function and blood–brain barrier maintenance. *EMBO J* **41**, e109890 (2022).
24. Fan, M. et al. Lactate promotes endothelial-to-mesenchymal transition via Snail1 lactylation after myocardial infarction. *Sci Adv* **9**, eadc9465 (2023).
25. Chen, J. et al. Lactate and lactylation in cancer. *Signal Transduct Target Ther* **10**, 38 (2025).
26. Jaworska, M. et al. The Warburg effect: A score for many instruments in the concert of cancer and cancer niche cells. *Pharmacol Rep* **75**, 876–890 (2023).
27. Huang, Y. et al. Improving immune-vascular crosstalk for cancer immunotherapy. *Nat Rev Immunol* **18**, 195–203 (2018).
28. Kane, K., Edwards, D. & Chen, J. The influence of endothelial metabolic reprogramming on the tumor microenvironment. *Oncogene* **44**, 51–63 (2025).
29. Leone, P. et al. Endothelial cells in tumor microenvironment: Insights and perspectives. *Front Immunol* **15**, 1367875 (2024).

Acknowledgements

We thank OE Biotech Co., Ltd., (Shanghai, China) for single-cell RNA-seq, spatial-resolved metabolomics and transcriptome sequencing used in this study, and acknowledge their Dr. Yuzhi Tan, Junhao Yu, Miao Shi, Zhenyu Xu, and Hengyun Wang for assistance with bioinformatics analysis. The present study was supported by the Natural Science Foundation of China (82303246), the Natural Science Foundation of Hunan Province (2023JJ41066,

2025JJ50493, and 2025JJ70052), Major Scientific Research Project for High-level Talents in Health Care of Hunan Province (R2023173) and Health Research Project of Hunan Provincial Health Commission (W20243173).

Author contributions

Y.Z. Tan, W.L. Tan, Y.C. Liang, and Y.Z. Long designed projects. S.H. Chen, Q.H. Hu, Y.J. Ou, J.L. Fu, and H. Chen collected tissue samples. F.Y. Ren, J. Ye, Q. Zhou, S. Li, and X.J. He analyzed the data. Q.Q. Wang, Y.M. Shen, and H.Y. Lu performed immunofluorescence staining. D.C. Wu, A.B. Gao, X. Chen and Y.K. Li revised the manuscript. All authors contributed to the article and approved the submitted version.

Competing interests

The authors declare no competing interests.

Additional information

Supplementary information The online version contains supplementary material available at <https://doi.org/10.1038/s41746-025-02286-7>.

Correspondence and requests for materials should be addressed to Daichao Wu, Anbo Gao, Xun Chen or Yukun Li.

Reprints and permissions information is available at <http://www.nature.com/reprints>

Publisher's note Springer Nature remains neutral with regard to jurisdictional claims in published maps and institutional affiliations.

Open Access This article is licensed under a Creative Commons Attribution-NonCommercial-NoDerivatives 4.0 International License, which permits any non-commercial use, sharing, distribution and reproduction in any medium or format, as long as you give appropriate credit to the original author(s) and the source, provide a link to the Creative Commons licence, and indicate if you modified the licensed material. You do not have permission under this licence to share adapted material derived from this article or parts of it. The images or other third party material in this article are included in the article's Creative Commons licence, unless indicated otherwise in a credit line to the material. If material is not included in the article's Creative Commons licence and your intended use is not permitted by statutory regulation or exceeds the permitted use, you will need to obtain permission directly from the copyright holder. To view a copy of this licence, visit <http://creativecommons.org/licenses/by-nc-nd/4.0/>.

© The Author(s) 2025

¹Department of Infectious Disease, Zhuzhou Hospital Affiliated to Xiangya School of Medicine, Central South University, Zhuzhou, Hunan, China. ²Zhuzhou Hospital Affiliated to Xiangya School of Medicine, Central South University, Zhuzhou, Hunan, China. ³Tumor ImmunoMetabolism Institute (TIMI), Zhuzhou Hospital Affiliated to Xiangya School of Medicine, Central South University, Zhuzhou, Hunan, China. ⁴Department of Respiratory and Critical Care Medicine, Zhuzhou Hospital Affiliated to Xiangya School of Medicine, Central South University, Zhuzhou, Hunan, China. ⁵Hunan Traditional Chinese Medical College, Zhuzhou, Hunan, China. ⁶Department of Cardiothoracic Surgery, Changde Hospital Affiliated to Xiangya School of Medicine, Central South University, Changde, Hunan, China. ⁷Department of Rehabilitation Medicine, Zhuzhou Hospital Affiliated to Xiangya School of Medicine, Central South University, Zhuzhou, Hunan, China. ⁸Trauma Center, Zhuzhou Hospital Affiliated to Xiangya School of Medicine, Central South University, Zhuzhou, Hunan, China. ⁹Department of Oncology, Zhuzhou Hospital Affiliated to Xiangya School of Medicine, Central South University, Zhuzhou, Hunan, China. ¹⁰Department of Radiology, Zhuzhou Hospital Affiliated to Xiangya School of Medicine, Central South University, Zhuzhou, Hunan, China. ¹¹Clinical Laboratory Department, Xiangya hospital, Central South University, Changsha, Hunan, China. ¹²Hunan Vigorzo Biotechnology Co., Ltd, Changsha, Hunan, China. ¹³The First Affiliated Hospital, Laboratory of Structural Immunology, Hengyang Medical School, University of South China, Hengyang, Hunan, China. ¹⁴Clinical Research Institute, The Second Affiliated Hospital, University of South China, Hengyang, Hunan, China. ¹⁵These authors contributed equally: Yingzheng Tan, Wenliang Tan, Yanchao Liang, Yunzhu Long, Shuanghua Chen. ✉ e-mail: wudaichao@usc.edu.cn; gaoanbo@usc.edu.cn; chenxun@csu.edu.cn; yukun_li@csu.edu.cn